Universidad Nacional Autónoma de México

Programa De Posgrado En Astrofísica

Instituto de Radioastronomía y Astrofísica

Emisión De Altas Energías De Brotes De Rayos Gamma

para optar por el grado de

Maestro En Ciencias (Astrofísica)

presenta

Mauricio González Servín

tutores

Estela Susana Lizano Soberón

Ramandeep Gill

Instituto de Radioastronomía y Astrofísica

Morelia,Mich. Octubre, 2023

Abstract

The origin of very high energy (VHE) afterglow emission in gamma-ray bursts (GRBs) is not fully understood. Spectral modeling of the broadband (radio to TeV) afterglow emission of TeV-bright GRBs can improve understanding of the shock microphysics at relativistic collisionless shocks and reveal the true energy budget of GRB jets. In this thesis work, a methodology is presented to fit the broadband afterglow observations of GRB 190114C, the first TeV-bright GRB reported in the literature, using a numerical code. To simulate the afterglow emission from an external forward shock a one-zone kinetic code is used that solves the coupled integro-differential equations for electrons (and $e^{\pm}$ pairs) and photons in the fluid frame. Observer frame quantities are then obtained by integrating over the equal-arrival-time surface in post-processing. To assess the importance of different high-energy processes, mainly three simulations were carried out, where (i) different physical processes such as synchrotron radiation, synchrotron self-Compton, production and annihilation of pairs, and Coulomb scattering are included, (ii) the effects of pair production are deactivated, and (iii) Coulomb interaction among electrons (and positrons) was disabled. The main conclusions of this thesis work are: (1) the TeV afterglow emission cannot be produced by synchrotron emission alone and an additional high-energy spectral component is required. As modeled in this work, this VHE emission can be synchrotron self-Compton (SSC) that arises naturally; (2) it is found that to have a detectable SSC component it is necessary to have a Compton-Y parameter greater than unity, with the condition that the fraction of the shock internal energy deposited in magnetic fields is much smaller than that deposited in electrons, i.e, $\epsilon_B \ll \epsilon_e$. The shock microphysical parameters obtained here are consistent with those obtained for other GRBs that are not TeV-

bright in the literature, which suggests that it does not require special conditions to produce TeV emission; (3) the problem of parameter space degeneracy is evident when comparing with other works, this is because different assumptions and the inclusion of different physical processes lead to varied model parameters, thus it is necessary to fit a sample of TeV-bright GRBs using a single model to obtain consistent results.

Resumen

Los brotes de rayos gamma (BRG) son los fenómenos más energéticos y luminosos observados en galaxias distantes del Universo. Los BRG son propulsados por chorros ultra-relativistas y se espera que sean fuentes de señales no electromagnéticas como los rayos cósmicos, los neutrinos y las ondas gravitacionales. Los BRG tienen dos fases principales de emisión y están basadas en la ubicación física donde se emiten los fotones de rayos-γ. La primera fase es la llamada "prompt emission", la cual está relacionada con la emisión del chorro desde un sitio "interno" a éste. La segunda fase, llamada "afterglow", es la que se estudia en esta tesis. Esta fase relacionada con la emisión de un sitio "externo" que resulta del medio externo chocado y barrido por la expulsión relativista. Por lo general, el afterglow ocurre al final de la "prompt emission", pero puede superponerse con ella. El afterglow ocurre en escalas de tiempo relativamente largas, con una duración de días, meses e incluso años y su emisión es de banda ancha, cubriendo ampliamente el espectro desde radio hasta los rayos-γ.
El origen de las emisiones del "afterglow" de muy alta energía (rango de energía de 0.1-1 TeV) en los brotes de rayos gamma no se entiende completamente. Debido a la larga duración de esta emisión, estudiar el modelado espectral de banda ancha (radio a TeV) en los BRG brillantes (TeV) puede mejorar la comprensión de la microfísica en los choques relativistas sin colisión, y revelar la verdadera estimación de energía de los chorros de los BRG. El modelado espectral sirve para estudiar los diferentes procesos radiativos, por ejemplo, leptónicos y hadrónicos, que son capaces de producir la emisión del "afterglow" de muy alta energía en los BRG. También impone importantes restricciones a la física de los BRG que no se pueden obtener solo de la emisión de sub-MeV. Naturalmente, esto nos hace preguntarnos por qué algunos

de los BRG más energéticos no se han observado en las energías TeV, y también lo que hace que otros TeV sean brillantes. Se cree ampliamente que la emisión del "afterglow" de TeV proviene de la emisión de sincrotrón auto-Compton. No se entiende por qué en los "afterglows" de muy alta energía se detectan fotones ≥ 10 GeV en varios BRG a tiempos tardíos ($t \sim 10^2$-10^3 s). Estos a menudo son difíciles de explicar con el modelo canónico de emisión de sincrotrón de un solo componente. Por lo tanto, se requiere de una componente espectral adicional de alta energía que puede ser explicada por el proceso sincrotrón auto-Compton o por modelos hadrónicos. En ese sentido, se utilizó un modelo leptónico para explicar esta componente de alta energía del "afterglow". Principalmente, se presenta una metodología para ajustar las observaciones de banda ancha del "afterglow" del GRB 190114C, que es el primer BRG brillante en TeV reportado por la literatura. Para simular la emisión del "afterglow" de un choque externo hacia adelante, se utiliza un código numérico cinético que resuelve las ecuaciones integro-diferenciales acopladas para electrones (y pares $e^{\pm}$) y fotones en el marco de referencia del fluido. Las cantidades en el marco del observador son obtenidas en un post-proceso integrando sobre la superficie de igual tiempo de llegada. Para evaluar la importancia de los diferentes procesos de alta energía se llevaron a cabo principalmente tres simulaciones, donde (i) se incluyen diferentes procesos físicos como la radiación sincrotrón, sincrotrón auto-Compton, la producción y aniquilación de pares, así como la dispersión de Coulomb, (ii) se desactivan los efectos de la producción de pares y (iii) se desactivó la interacción de Coulomb entre electrones (y positrones). Las principales conclusiones de este trabajo de tesis son: (1) la emisión del "afterglow" de TeV no se puede producir solo por la emisión de sincrotrón, también se requiere una componente espectral adicional de alta energía. Como se modela en este trabajo, esta emisión de muy alta energía puede ser el proceso de sincrotrón auto-Compton que surge de forma natural; (2) se encuentra que para tener un componente sincrotrón auto-Compton detectable es necesario tener un parámetro Y-Compton mayor que la unidad, con la condición de que la fracción de la energía interna de choque depositada en los campos magnéticos sea mucho más pequeña que la depositada en los electrones, es decir, $\epsilon_B \ll \epsilon_e$. Los

parámetros microfísicos de choque obtenidos aquí son consistentes con los obtenidos para otros BRG que no son TeV brillantes en la literatura, lo que sugiere que no se requiere condiciones especiales para producir la emisión de TeV; (3) el problema de la degeneración del espacio de parámetros es evidente cuando se compara con otros trabajos, debido a que las diferentes suposiciones y la inclusión de diferentes procesos físicos conducen a parámetros de modelo variados, por lo que es necesario ajustar una muestra de BRG brillantes de TeV utilizando un solo modelo para obtener resultados consistentes.

Contents

Abstract **ii**

Resumen **iv**

1 Introduction **1**

2 Phenomenology of Gamma-Ray Bursts **6**

2.1 Prompt Emission 6

2.2 Afterglow 10

3 Relativistic fluids **16**

3.1 Relativistic Hydrodynamics 16

3.2 Equation of State 17

3.3 Shock Jump Conditions 18

3.4 Cold Upstream Fluid 19

3.5 Shock parameterization 21

4 Radiative processes **23**

4.1 Synchrotron Radiation 23

4.1.1 Emission in a Magnetic Field 23

4.1.2 Synchrotron Cooling 27

4.1.3 Synchrotron Self-Absorption 30

4.1.4 Broken Power-Law Spectra 31

4.2 Synchrotron Self-Compton (SSC) 34

4.3 Pair Production 38

5 Afterglow model **40**

5.1 Dynamics in the Self-Similar Regime 40

5.2 Blandford-Mckee Self-Similar Solution 41

5.3 Dynamics of a thin shell 42

5.4 Afterglow Emission 44

6 Numerical Simulations **48**

6.1 Numerical Method 48

6.2 The observed radiation 51

6.3 Analytic vs. Numerical 53

6.4 GRB 190114C 55

6.5 Comparison with Other Works 61

7 Conclusions **68**

7.1 Future Work 69

Appendix A Numeric Code Details **71**

A.1 Adiabatic cooling and density dilution 71

A.2 Compton scattering 73

A.3 Pair production and annihilation 73

A.4 Coulomb Scattering 74

Bibliography **74**

List of Figures

1.1 Canonical GRB fireball model. Figure of NASA's Goddard Space Flight Center (2023). 3

2.1 The GRBs bimodal distribution are divided into two classes at $T_{90} = 2$ s (vertical line): LGRBs (dotted line) and SGRBs (dashed line). Figure 1 of Zhang and Choi (2008). 8

2.2 Examples of lightcurves. Figure 6 of Fishman et al. (1994). 8

2.3 Example for the GRB 990123 prompt emission spectrum. Figure 1 of Briggs et al. (1999). 11

2.4 Example of three spectral components. Where (I) is a Band-function component, (II) is a quasi-thermal component, and (III) is an extra power-law component. Figure 23 of Zhang et al. (2011) 11

2.5 Example of multi-wavelength light curves (from radio to gamma rays) of GRB 190114C. The dashed vertical line roughly marks the end of the prompt emission phase and the beginning of the afterglow. Energy flux versus time after the BAT trigger (at $T_0 = 20 : 57 : 03.19$ universal time). Figure 1 of Veres et al. (2019). 14

2.6 A canonical X-ray afterglow lightcurve showing five distinct temporal components: I. steep decay phase; II. shallow decay phase (or plateau if the decay slope is close to 0); III. normal decay phase; IV. post-jet-break phase; V. flares. The segment "0" denotes the prompt emission phase. Figure adapted from Zhang et al. (2006). 15

3.1 Scheme of upstream flow (region I) and downstream flow (region II) shown in a frame in which the shock is at rest. 18

4.1 Synchrotron spectrum in slow cooling regime for a power-law electron distribution (Figure 1b of Sari et al. (1998)) 33
4.2 Synchrotron spectrum in fast cooling regime for a power-law electron distribution (Figure 1a of Sari et al. (1998)) 34
4.3 Example of synchrotron (left) and SSC (right) spectrum. The regime is fast cooling. 38
4.4 Two-photons pair production. 39

6.1 A 2D cross-section of a 3D equal-arrival-time surface (EATS) for a relativistic spherical shell (e.g., Zhang, 2018). Photons emitted along the EATS at different angles away from the line-of-sight, and correspondingly from different radii and at different lab-frame times, arrive at the distant observer at the same time. 52
6.2 Comparison of spectra obtained with numerical and analytical models. The parameters are shown in Table 6.1. 54
6.3 GRB 190114C spectrum for different times (after correction for extinction due to the extragalactic background light). The black lines are the simulations and the green regions are the 1σ error regions of the data in different energy bands collected by different detectors of MAGIC (2019). The red curves are the case with $\kappa = 20.0$ and the blue-light curves are the case with $\kappa = 10.0$. 58
6.4 GRB 190114C spectrum at 75 seconds. Only the synchrotron part (blue dashed line). Only synchrotron self-Compton part (red dashed line), and total spectrum (black line). 59
6.5 The black curves are GRB 190114C spectrum at 75 seconds (a) and 140 seconds (b), but with pair production and pair annihilation processes disabled in the numerical simulation. The red dashed curves are the original spectra of figure 6.3. 60

6.6 Light curve of GRB 190114C. Green points enclose the 1σ error region of the MAGIC data (0.3-1 TeV) and the black line is the lightcurve from the numerical simulation for $E = 0.3 - 1\,\mathrm{TeV}$. 60

6.7 Relative errors vs. energy for the different models, for data in the range 68-110 seconds). 64

6.8 GRB 190114C model spectra from different works. The black curve shows the spectrum obtained from the numerical model in this thesis for parameters different from that in the works compared here (see Table 6.2). Panel (a) shows the spectrum from Asano et al. (2020) (blue light line). Panel (b) shows the spectrum from Veres et al. (2019) (blue line). Panel (c) shows the spectrum from Joshi and Razzaque (2021) (green line). Panel (d) shows the spectrum from Derishev and Piran (2021) (red line). 66

6.9 GRB 190114C spectrum. The light-blue curve is the spectrum from Asano et al. (2020) for an ISM external medium (method I in their paper). The black curve is the spectrum obtained by the numerical model used in this thesis for the same parameters as Asano et al. (2020). 67

1 Introduction

Gamma-ray bursts (GRBs) are electromagnetically the most luminous phenomena in the universe, where they outshine the entire γ-ray sky during the most intense phase of their emission (e.g., Vedrenne and Atteia, 2009). They are powered by ultra-relativistic jets (Nakar, 2015), and theoretical arguments and observational evidence suggest that GRBs must have bulk Lorentz factors larger than ~ 100 and even up to ~ 3000 (e.g., Fishman and Meegan, 1995; Piran, 2005). The isotropic-equivalent γ-ray luminosity of the initial most intense phase is on the order of $10^{51} - 10^{54}$ erg s^{-1} (e.g., Paczyński, 1998) making it possible to observe GRBs to cosmological distances (redshifts $z \geq 8$),(e.g., Lamb and Reichart, 2000). GRBs are also expected to be sources of non-electromagnetic signals, including cosmic rays, neutrinos, and gravitational waves (e.g., Mészáros et al., 2003). Gravitational waves were finally detected in coincidence with the GRB itself in the binary merger of two neutron stars in the source GW170817 (e.g., Abbott et al., 2017a,b). No high-energy neutrinos have been observed from GRBs yet.

The cosmological principle tells us that the Universe is homogeneous and isotropic on a large scale (e.g., Liddle, 1998), therefore, as GRBs are cosmological sources, their distribution is also expected and observed to be isotropic and homogeneous (e.g., Horváth et al., 2014; Andrade et al., 2019). Due to the extreme physical conditions in which they originate, GRBs provide us with a cosmological laboratory, directly related to various branches of astrophysics. Their high-velocity, high-energy environment, strong gravity, and strong electromagnetic fields make them some of the most interesting and complex phenomena today. After decades of observational and theoretical studies, we have managed to arrive at a physical picture of the origin of

GRBs. Due to the complexity of these phenomena, many details remain unclear, but a general theoretical framework has been established that is considered successful in interpreting multi-wavelength data.

GRBs have two main phases of emission based on the physical location where the γ-ray photons are emitted (e.g., Nakar, 2007). The first phase is the so-called "prompt emission", and this phase is related to jet emission from a site "internal" to the jet, such as in internal shocks (e.g., Mészáros and Rees, 1994; Sari and Piran, 1997). During this short-lived phase, with duration ranging from milliseconds to hundreds of seconds (Zhang and Meszaros, 2004; Zhang, 2018), most of the γ-ray photons are emitted in the keV–MeV bands (γ-rays/hard X-rays) with a mean energy of $\sim (200 - 500)\,\mathrm{keV}$ (e.g., Goldstein et al., 2012; Gruber et al., 2014). Based on the duration distribution, GRBs are classified in two ways (e.g., Kouveliotou et al., 1993): short-duration GRBs (lasting less than two seconds) and long-duration GRBs (lasting more than two seconds). Long GRBs are thought to be associated with the core-collapse of massive stars with masses between 20 and 30 $M_{\odot}$(e.g., Woosley, 1993), as also inferred from the Type Ic spectra of the associated supernovae (e.g. Stanek et al., 2003). Short GRBs are believed to be generated by mergers of compact objects (e.g., Belczynski et al., 2006), i.e. black holes and neutron stars, and after GW170817 one now knows that at least some are produced by the mergers of neutron stars and neutron stars as predicted (e.g., Narayan et al., 1992; Eichler et al., 1989). In both types of GRBs, the remnant is either a hyperaccreting stellar-mass black hole or a rapidly rotating highly magnetized neutron star, known as a millisecond magnetar (e.g., Thompson and Duncan, 1993), serving as the engine to drive the collimated outflow (jet) up to relativistic velocities.

The second phase is the so-called "afterglow" (e.g., Mészáros, 2001), and is related to emission from an "external" site, such as the shocked external medium swept up by the relativistic ejecta (e.g., Zhang et al., 2006; Nava et al., 2013). It generally occurs at the end of the prompt emission but it can also overlap with it. It is long-lasting with duration from days, months, to years (e.g., Zhang, 2018), and its emission is broad-band, covering from radio, millimeter (mm), infrared (IR), optical, ultraviolet

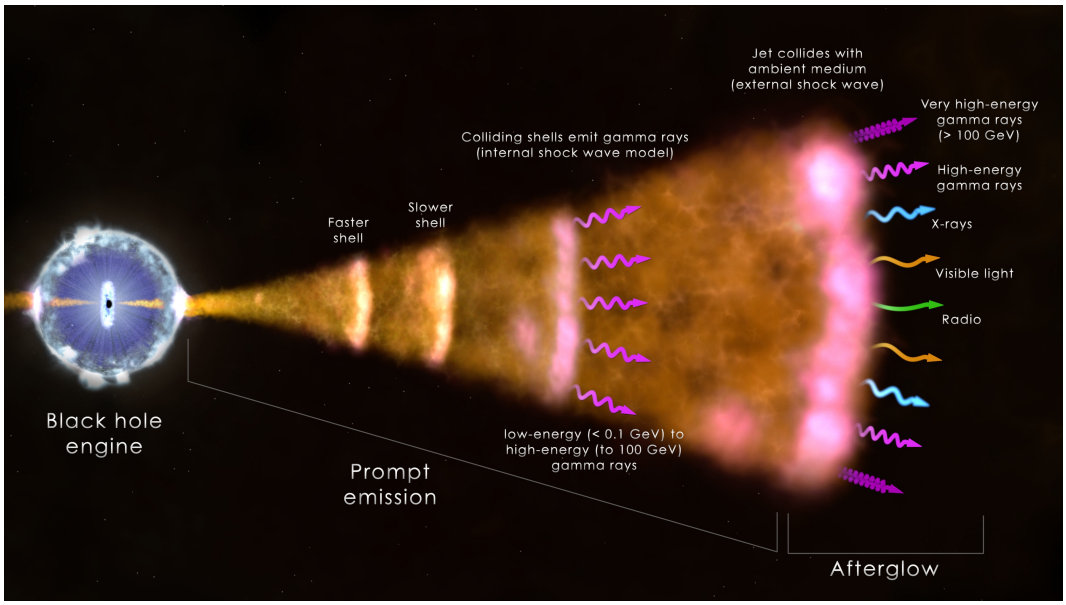

Figure 1.1: Canonical GRB fireball model. Figure of NASA's Goddard Space Flight Center (2023).

(UV), X-rays, and even gamma rays (e.g., Zafar, 2011; Zhang, 2018). This emission can come from the forward shock propagating ahead of the relativistic ejecta and into the external medium and/or the reverse shock propagating into the jet itself (see Figure 1.1). In these two shocks, small-scale magnetic fields are generated, and electrons and protons are accelerated This results in bright broad-band non-thermal emission produced by synchrotron radiation and synchrotron self-Compton emission in the high-energy band (e.g., Ghisellini et al., 1998; Arimoto et al., 2016).

Over the last few years, research in GRB physics has become more active and interesting with the detection of Very-High-Energy (VHE) afterglow emission in the 0.1-1 TeV energy range with ground-based atmospheric Cherenkov telescopes that are effective instruments for very high-energy γ-radiation observations of physical phenomena. (e.g., Ferenc et al., 2005; Konopelko and Plyasheshnikov, 2000). Before that, all GRBs had been detected up to a few MeV, and many with energies up to several tens of GeV with the help of the Fermi Large Area Telescope (LAT) (e.g., Ajello et al., 2019). Due to the long duration of the afterglow emission, long-term multi-waveband data are available to study the different radiative processes, e.g. leptonic and hadronic, that are capable of producing VHE afterglow emission in GRBs. Its

study is important because it provides crucial information about the global energy budget of these bursts. It also imposes important constraints on the physics of GRBs that cannot be obtained from sub-MeV emission alone. There are MeV-bright GRBs that have not been observed at TeV energies after the ground-based TeV detectors became operational. Naturally, this raises the question why some of the most energetic GRBs have not been observed at TeV energies (e.g., GRB 130427A), and what makes others TeV-bright. The TeV afterglow emission is widely believed to be synchrotron self-Compton (e.g., Chiang and Dermer, 1999). Several works have modeled this emission using analytical models (e.g., Sari and Esin, 2001; Yamasaki and Piran, 2022), but they remain incomplete as they ignore the effects of electron-positron pair cascades and Klein-Nishina suppression (e.g., Asano and Mészáros, 2012; Vurm et al., 2011), that are important for understanding the multi-wavelength spectral and temporal evolution, and can shed more light on the properties of the emission region. Another important open question related to the high-energy afterglow emission seen by Fermi-LAT is the detection of ≥ 10 GeV photons in several GRBs at late times ($t \sim 10^2 - 10^3$ s). These are often difficult to explain with the canonical single-component synchrotron emission model. Therefore, either an additional high-energy spectral component is required or the origin of these photons must be different, e.g., hadronic (Böttcher and Dermer, 1998).

In this work I study the afterglow emission through numerical simulations with the numerical code developed by Gill and Thompson (2014), assuming that there is an external shock between the ejecta and the circumburst medium, where I assume that several processes take place such as the synchrotron, synchrotron self-Compton, production and annihilation of pairs, among others. In addition, to calculate the observed flux density, an integration is implemented on the equal arrival time surface. This thesis consists of seven chapters, where chapter two presents a brief explanation of all the observational properties of GRBs that we know of. Chapter three presents the hydrodynamic equations that describe relativistic jets. In chapter four, I will present some radiative processes that are present in GRBs. Chapter five contains the coupling of the dynamics with the radiative processes for the afterglow emission, I

also present the numerical code that I use to carry out the simulations. In chapter six I will present the results of the numerical simulations, and finally in chapter seven I will give the conclusions.

2 Phenomenology of Gamma-Ray Bursts

This chapter will provide a summary of all the observational clues that we know about GRBs, since, in order to apply known physical laws and logical reasoning, it is vital to collect as much observational data as possible. This first step is essential to be able to understand what physical processes are those that produce gamma-ray bursts. The type of GRB data that we know of are, for example, the observational properties of prompt emission and afterglow, the association of a supernova (kilonova) with a long (or short) GRB (e.g., Kumar and Zhang, 2015; Zhang, 2018). This chapter will mainly show the observational properties of prompt emission and afterglow, as it is a very extensive topic.

2.1 Prompt Emission

The phase called prompt emission is mainly observed in the gamma-ray energy range 0.1-2 MeV. In the following points I will highlight the main characteristics of this phase.

Temporal properties:

- Duration: As mentioned above, the GRBs show a bimodal distribution. GRBs that are longer than 2 seconds are classified as "long GRBs", and GRBs that are shorter than 2 seconds are referred to as "short GRBs". The burst duration is defined by the time interval called T_{90} between the epochs when 5% and 95% of a total fluence is registered by a detector (see Figure 2.1). (see for details Zhang and Meszaros, 2004; Zhang and Choi, 2008; Kumar and Zhang, 2015).

- The lightcurves: GRB lightcurves are very variable and irregular in general, comprising single or multiple overlapping pulses. Some lightcurves are extremely variable while others can be very smooth (e.g., Fishman and Meegan, 1995). For an example see the Figure 2.2.

- Null Periodicity: The Power Density Spectrum (PDS, (e.g., Beloborodov et al., 2000; Maral, 2004)) study revealed that the lightcurves of GRBs display null periodicity, suggesting that the central engine of GRBs does not display apparent periodic behavior. It may also be that the central engine has a periodic behavior but is lost during the time the ejecta travels and generates the emission (e.g., Beskin et al., 2010; Zhang et al., 2016). Individual PDSs can be very noisy. However, averaging the PDS of several bright GRBs display a power law exponent of approximately $-5/3$ (e.g., Beloborodov, 2000).

- Precursor emission: Some GRBs have a softer and weaker "precursor" emission, that is well separated from the main burst by 10 to 100 seconds (e.g., Lazzati, 2005; Burlon et al., 2009).

- Pulse widths: The widths of individual pulses can vary in a wide range. For example, for pulses that have a smaller peak, the widths (i.e. δt) are milliseconds or even less than milliseconds, basically, this measure gives the variability timescale of the prompt emission. In general, the pulses tend to be wider in the softer energy bands and narrower in the harder energy bands (e.g., Zhang and Meszaros, 2004; Zhang, 2018).

- Asymmetries: The shape of many individual pulses is often asymmetric in their lightcurves, with a steep rising phase and a shallower downward phase. Although several functional ways have been proposed to fit the pulses shapes, the most widely used for some bright and isolated pulses is modeled by a fast-rise-exponential-decay (FRED) function (e.g., Kumar and Zhang, 2015; Zhang, 2018).

Spectral Properties

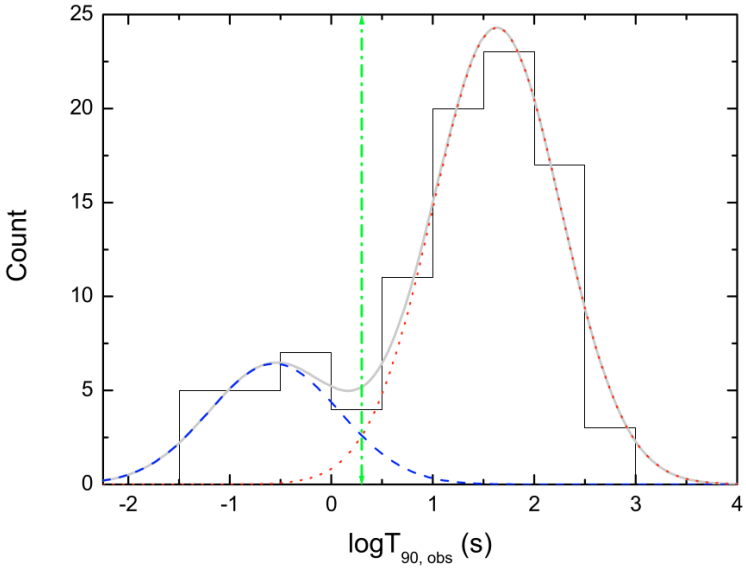

Figure 2.1: The GRBs bimodal distribution are divided into two classes at $T_{90} = 2$ s (vertical line): LGRBs (dotted line) and SGRBs (dashed line). Figure 1 of Zhang and Choi (2008).

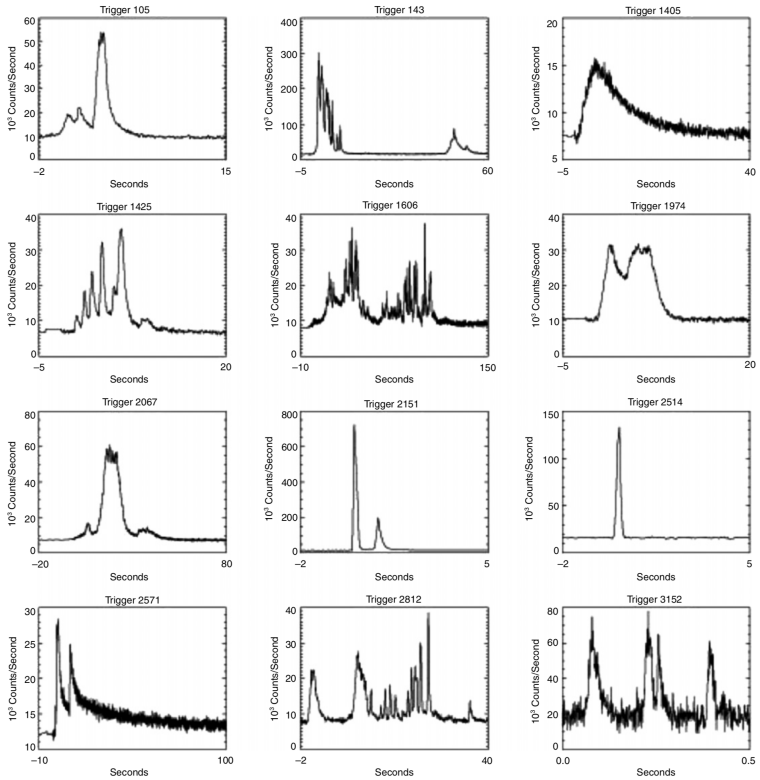

Figure 2.2: Examples of lightcurves. Figure 6 of Fishman et al. (1994).

- Non-thermal spectrum: The continuum spectrum is non-thermal and features a smoothly broken power law, often modelled using an empirical relation known as the "Band-function" (e.g., Band et al., 1993) (see Figure 2.3). The photon number spectrum

$$N(E) = \begin{cases} A\left(\frac{E}{100\mathrm{keV}}\right)^{\alpha} \exp -\frac{E}{E_0} & \text{for} \quad E < (\alpha-\beta)E_0, \\ \\ A\left(\frac{(\alpha-\beta)E_0}{100\mathrm{keV}}\right)^{\alpha-\beta} \exp\left(\beta-\alpha\right)\left(\frac{E}{100\mathrm{keV}}\right)^{\beta} & \text{for} \quad E \geq (\alpha-\beta)E_0, \end{cases} \tag{2.1}$$

  where $N(E)dE$ is the number of photons in the energy bin dE, A is the normalization of the spectrum, E_0 is the break energy in the spectrum and, α and β are the photon spectral indexes below and above the break energy E_0. The peak energy in the $E^2N(E)$ spectrum is called the E peak (E_p), which is related to E_0 through $E_p = (2+\alpha)E_0$.

- Classification: From hard to soft, the bursts can sometimes also be classified as gamma-ray bursts ($E_p > 50$ keV), X-ray rich GRBs (XRGRB, 30 keV $< E_p <$ 50 keV), and X-ray flashes (XRFs, $E_p < 30$ keV), without a clear boundary in between (e.g., Sakamoto et al., 2008). The bimodality is also confirmed spectrally, because short GRBs are predominantly harder, and long GRBs tend to be softer in their spectral peak energies (e.g., Kouveliotou et al., 1993).

- Thermal component: For the vast majority of bursts, a thermal spectrum (like Planck's) is not expected. Most are better modeled with the classic Band-function. A small fraction of GRBs display a (quasi-) thermal component superposed on top of a non-thermal component (e.g., Zhang et al., 2011; Zhang, 2018).

- High-energy component: For some GRBs, in addition to having thermal and band components, it is necessary to include another high-energy spectral component to accommodate the broad-band spectra(e.g., Abdo et al., 2009; Acker-

mann et al., 2010; González et al., 2003). One of the main characteristics of this component is that it follows a power law that extends to the Fermi LAT band at high energies (above 100 MeV), but sometimes also extends to low energies (in the X-ray Band). The slope is almost always positive in the νF_ν spectrum and to avoid an energy divergence there must be a spectral break at high energies which is not seen.

In general, the prompt emission spectrum of GRBs may include three elementary spectral components (e.g., Zhang et al., 2011): (I) a non-thermal Band component; (II) a quasi-thermal component; and (III) another non-thermal component that extends to high energies (see Figure 2.4). Which component will dominate the spectrum can vary between GRBs. It is possible that all three components exist in at least some GRBs (e.g., Guiriec et al., 2015). It is not clear what is the physical origin of the three spectral components, but the thermal component is thought to be due to photospheric emission (e.g., Pe'er et al., 2006), i.e when the ejecta becomes optically thin, while the Band component is due to non-thermal synchrotron radiation in the optically thin region (e.g., Zhang et al., 2012). The high energy component is the one we know least about.

2.2 Afterglow

After the prompt emission, the afterglow emission phase follows, which was even predicted before its discovery (e.g., Paczynski and Rhoads, 1993; Katz, 1992; Mészáros and Rees, 1997). Regardless of what the GRB's central engine is (black hole or a millisecond magnetar (e.g., Lü et al., 2015), it produces a huge amount of energy in a small region of space, that turns into a fireball expanding at relativistic speeds (e.g., Meszaros and Rees, 1993). Due to a small amount baryons in the fireball (that assumes a weakly magnetized outflow) (e.g., Meszaros and Rees, 1993; Lazzati and Begelman, 2010), its internal energy is transformed into the kinetic energy of the ejected matter when the fireball is optically thick. One knows that there must be interstellar gas in the host galaxy, which gradually slows down the ultra-relativistic

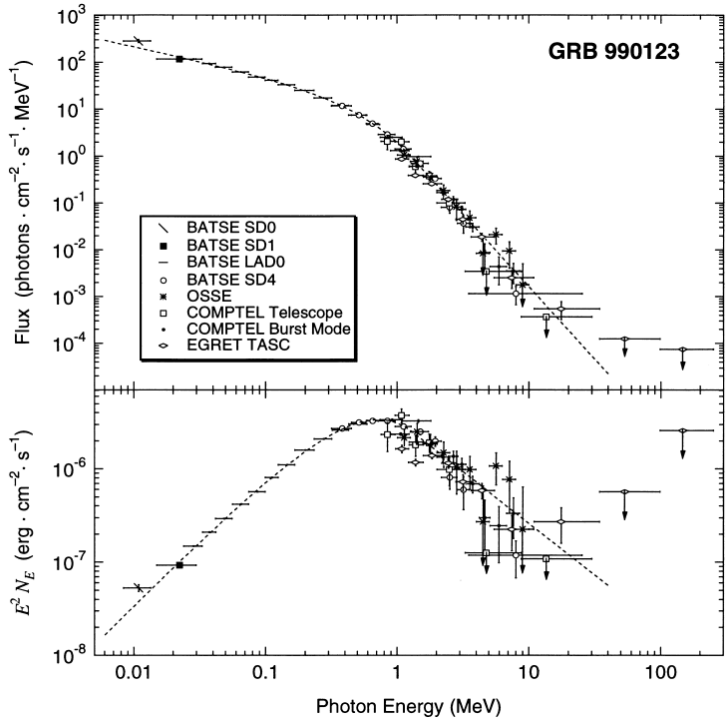

Figure 2.3: Example for the GRB 990123 prompt emission spectrum. Figure 1 of Briggs et al. (1999).

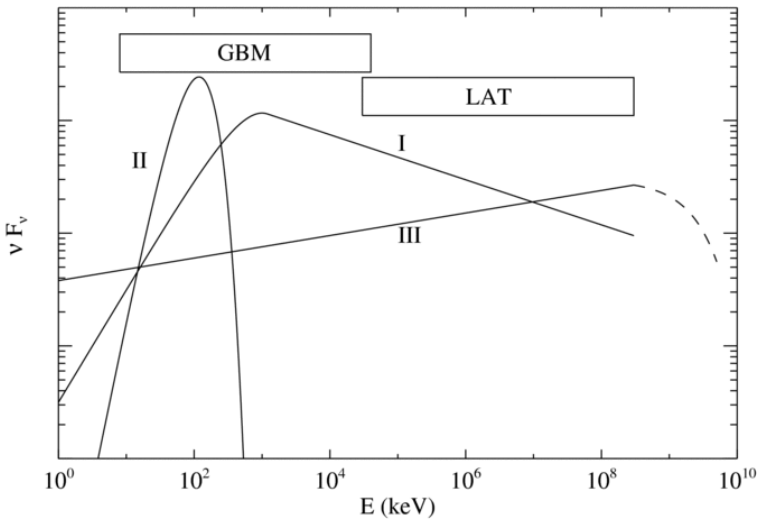

Figure 2.4: Example of three spectral components. Where (I) is a Band-function component, (II) is a quasi-thermal component, and (III) is an extra power-law component. Figure 23 of Zhang et al. (2011)

ejecta as it sweeps up the circumburst medium, generally due to a forward shock and also a reverse shock that penetrates the ejecta (e.g., Zhang and Kobayashi, 2005). What happens in the shocks is that the electrons (and protons) would be accelerated, producing bright broad-band non-thermal emission via synchrotron (in the shock-generated small scale magnetic field) and synchrotron Self-Compton (SSC). As expected, as the fireball slows down, the force of the impact is reduced, so the emission softens and fades over time, i.e. the GRB fades. So, we can define afterglow emission as a broadband emission released during the interaction between the fireball ejection and the circumburst medium (e.g., Zhang, 2018). Although the emission is believed to come from external shocks, Swift's observations suggested that not all subsequent emission can be attributed to emission from external shocks. For example X-ray flares (see the Swift/BAT lightcurve in Figure 2.5 around $T - T_0 \sim 20\,\mathrm{s}$) are likely emission from an "internal" site in the jet, due to their short variability timescale with $\Delta T/T \ll 1$. In Mészáros and Rees (1997), they provide detailed and self-consistent predictions for the broad-band emission based on the external shock model. Currently, one has extensive afterglow data, where the main observational properties of afterglow radiation are (e.g., Kumar and Zhang, 2015):

Global properties:

- Optical afterglow follows a power law in which the flux decays as $F_\nu \propto t^{-\alpha}$, with decay rate $\alpha \sim 1$ (e.g., Wijers et al., 1997; Harrison et al., 1999), consistent with the prediction of the standard external shock afterglow model, for example see Figure 2.5 (e.g., Mészáros and Rees, 1997; Sari et al., 1998).

- A temporal break in the optical afterglow light curve is most often detected for bright GRBs, where the break time is about one day, so there is a steeper decline with slope $\alpha \sim 2$ (e.g., Harrison et al., 1999). This is consistent with the achromatic phenomenon called "jet break" which is caused by a geometric effect, i.e., when an on-axis observer "sees" the edge of the jet. (e.g., Piran et al., 1999; Rhoads, 1999; Zhang, 2018).

- The radio afterglow light curve initially increases to a maximum around 10 days,

then decays (e.g., Frail et al., 2000). The maximum peak normally corresponds to the passage of the synchrotron injection frequency ν_m, or the synchrotron self-absorption frequency ν_a, through the radio band.

- From radio to X-rays wavelengths, one can also fit the broad-band afterglow spectrum with a broken power law, at a fixed observer time (e.g., Harrison et al., 1999; Wijers and Galama, 1999), as expected for the synchrotron afterglow model.

- With high-quality data, bursts can be observed whose optical light curves show greater detail, such as bumps and ripples that deviate from the simple afterglow model predictions (e.g., Lipkin et al., 2004). The soft bumps in the afterglow light curves can be interpreted as being due to density bumps in the external medium (e.g., Lazzati et al., 2002; Dai and Wu, 2003; Nakar and Granot, 2007) while the sharper features in the light curves can be due to energy injection from the central engine(e.g., Kumar and Piran, 2000; Zhang and Mészáros, 2002), angular energy fluctuations per solid angle unit (e.g., Yamazaki et al., 2004; Kumar and Piran, 2000), or the existence of two-component jets (e.g., Berger et al., 2003; Racusin et al., 2008).

Basically, one can summarize the data with a canonical light curve, which usually includes 5 components, nevertheless not all GRBs display all 5 components. (e.g. Zhang et al., 2006; Nousek et al., 2006) (see Figure 2.6).

Characteristics of the components:

- I. Steep decay phase: it has a temporal decay $d\ln F_\nu / d\ln t < -2$. This phase may be simply the high latitude emission associated with the prompt gamma-ray source at $R \geq 10^{15}$ cm (distance from central engine to emission region) when the central engine is turned off faster than the decay of the X-ray light curve (e.g. Zhang et al., 2006; Nousek et al., 2006; Kumar and Panaitescu, 2000; Liang et al., 2006). If the emission region has a much smaller radius, the rapidly decaying X-ray light curve reflects the time dependence of central engine activity (e.g. Duran and Kumar, 2009; Fan and Wei, 2005).

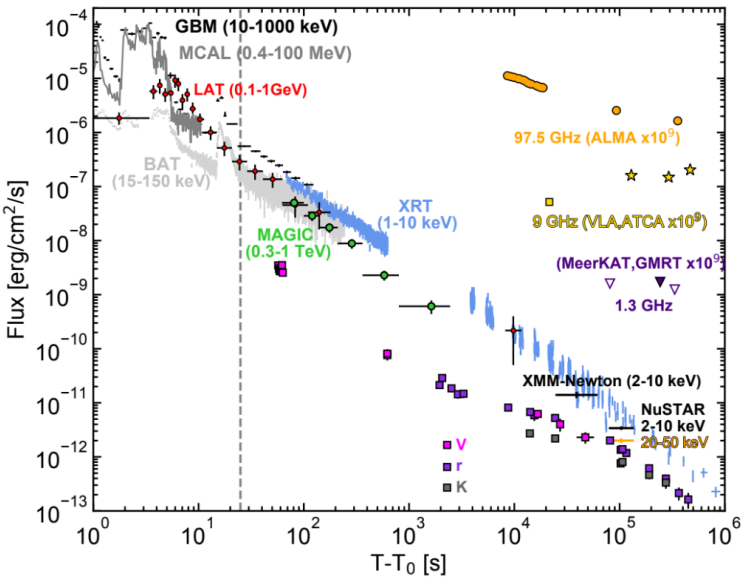

Figure 2.5: Example of multi-wavelength light curves (from radio to gamma rays) of GRB 190114C. The dashed vertical line roughly marks the end of the prompt emission phase and the beginning of the afterglow. Energy flux versus time after the BAT trigger (at $T_0 = 20:57:03.19$ universal time). Figure 1 of Veres et al. (2019).

- II. Shallow Decay Phase (or Plateau Phase): the temporary decay of the flux is shallow with a temporal slope of -0.5 or greater, sometimes flat or even slightly rising at first. In most GRBs, it is followed by a "normal" decay with flux decreasing with time as $\sim t^{-1}$.

- III. Normal decay phase: This is the typical decay ($\sim t^{-1}$) expected in the standard external-forward shock model (e.g., Wang et al., 2015).

- IV. Late steep decay phase ($\sim t^{-2}$ or steeper). Expected in the forward shock model (e.g., Panaitescu, 2007) after the jet break.

- V. X-ray flares: One or more X-ray flares can be found in about half of GRB X-ray afterglows. These flares share many properties with the prompt emitting pulses. It is widely accepted that they are driven by late central engine activity (e.g. Ioka et al., 2005; Burrows et al., 2005; Zhang et al., 2006; Fan and Wei, 2005; Chincarini et al., 2007; Lazzati and Perna, 2007; Liang et al., 2006).

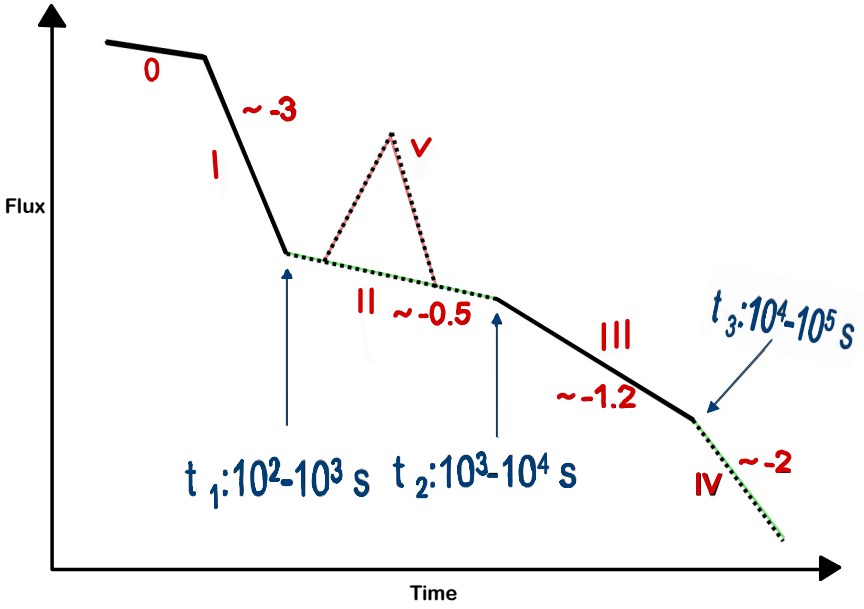

Figure 2.6: A canonical X-ray afterglow lightcurve showing five distinct temporal components: I. steep decay phase; II. shallow decay phase (or plateau if the decay slope is close to 0); III. normal decay phase; IV. post-jet-break phase; V. flares. The segment "0" denotes the prompt emission phase. Figure adapted from Zhang et al. (2006).

3 Relativistic fluids

In this chapter I present a brief review of relativistic fluid dynamics, because GRBs are produced by relativistic jets. In addition, the fluid equations help us to see another topic that will be described in this chapter, which is relativistic collisions. The GRB prompt and afterglow emission is interpreted as occurring in shocks.

3.1 Relativistic Hydrodynamics

Relativistic fluid equations are based on three conservation principles: conservation of energy and momentum in the energy-momentum tensor and conservation of number density. One defines the four-vector of position as $x^\mu = (ct, \mathbf{x})$, where t is the time in the lab-frame, $\mathbf{x}$ is the spatial coordinates vector, the proper time as $d\tau = dt/\gamma$, the four-velocity as $u^\mu = dx^\mu/(cd\tau) = \gamma(1, \mathbf{v}/c)$, where $\mathbf{v}$ is the 3-velocity, and the relative Lorentz factor between the two frames is $\gamma = 1/\sqrt{1-(v/c)^2}$, where c is the speed of light. Also one can define the four mass density as j^μ and energy-momentum tensor ($T^{\mu\nu}$) as (e.g., Zhang, 2018):

$$j^\mu = (j^0, \mathbf{j}) = \rho u^\mu, \tag{3.1}$$

$$T^{\mu\nu} = (\rho c^2 + \epsilon + p)u^\mu u^\nu + p\eta^{\mu\nu} = hu^\mu u^\nu + p\eta^{\mu\nu}, \tag{3.2}$$

where $h = \rho c^2 + \epsilon + p$ is the enthalpy density of the gas, $\eta^{\mu\nu}$ is the Minkowski metric, ρ, p and ϵ are the mass density, pressure and internal energy density, respectively. With these definitions we can write the equation of conservation of mass $\nabla_\mu j^\mu = 0$ and the conservation of energy-momentum as $\nabla_\mu T^{\mu\nu} = 0$, which are explicitly written

as:

$$\frac{\partial(\gamma\rho)}{\partial t} + \nabla \cdot (\gamma\rho\mathbf{v}) = 0, \tag{3.3}$$

$$\frac{\partial \mathbf{v}}{\partial t} + (\mathbf{v} \cdot \nabla)\mathbf{v} = -\frac{1}{\gamma^2 h}\left(c^2\nabla p + \mathbf{v}\frac{\partial p}{\partial t}\right), \tag{3.4}$$

$$\frac{\partial(\gamma^2 h)}{\partial t} - \frac{\partial p}{\partial t} + \nabla \cdot (\gamma^2 h\mathbf{v}) = 0, \tag{3.5}$$

These equations are known as the equations of conservation of mass, momentum, and energy, respectively.

3.2 Equation of State

Since we only have 5 differential equations (3.3)-(3.5), and six unknown variables (ρ, p, ϵ and three velocity components) we need to add another equation, which is called the equation of state. This equation tells how the pressure of the gas is related to other thermodynamic properties, as well as connecting the macroscopic world with the microscopic one. For a perfect fluid like an ideal gas we can write this relationship as

$$p = \kappa\epsilon, \tag{3.6}$$

where $\kappa \approx \frac{\bar{\gamma}+1}{3\bar{\gamma}}$, $\bar{\gamma}$ is the average Lorentz factor of the particle gas (e.g., Uhm, 2011). We can introduce the adiabatic index (e.g., Kumar and Granot, 2003; Uhm, 2011)

$$\hat{\gamma} = \frac{c_p}{c_v} = \frac{\epsilon + p}{\epsilon} = \kappa + 1 \approx \frac{4\bar{\gamma} + 1}{3\bar{\gamma}}, \tag{3.7}$$

where c_p and c_v are the specific heats. Introducing this adiabatic index is important since for perfect fluids, the system is adiabatic, that is, we can express the equation of state as

$$p \propto \rho^{\hat{\gamma}}, \tag{3.8}$$

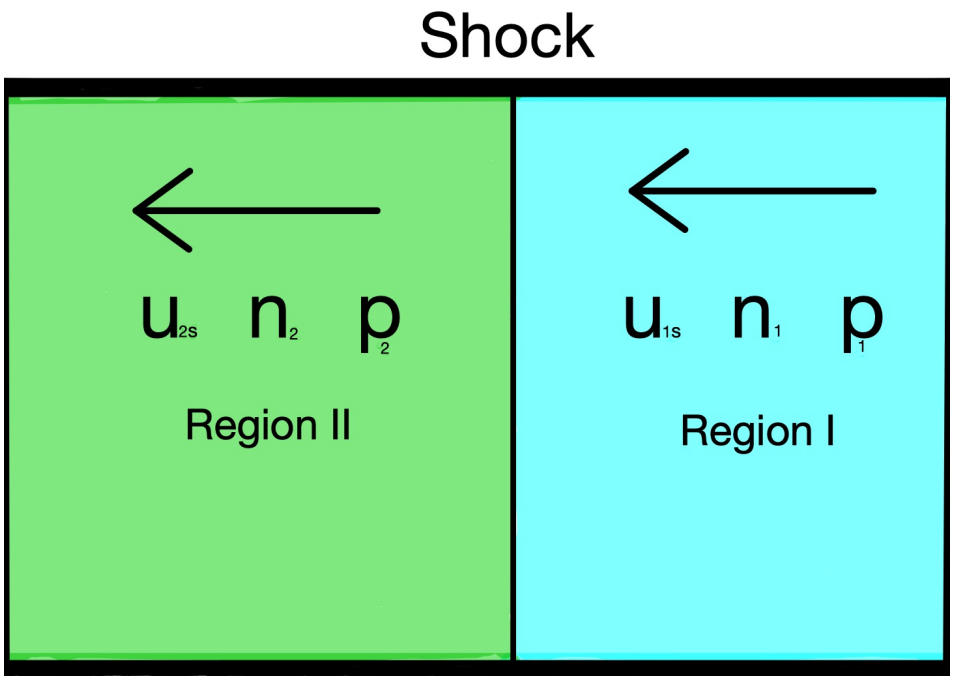

Figure 3.1: Scheme of upstream flow (region I) and downstream flow (region II) shown in a frame in which the shock is at rest.

3.3 Shock Jump Conditions

The equations that describe a discontinuity surface in the relativistic ideal gas are called Taub Adiabats equations or jump conditions (e.g., Zhang, 2018). The simplest case is when one has two regions, i.e. upstream and downstream across the shock where their properties are labeled 1 and 2, respectively (see figure 3.1). The properties of the downstream fluid can be linked to the properties of the upstream fluid using the shock jump conditions. To find these jump equations we use the principles of conservation of energy, mass and momentum assuming that the fluid is adiabatic. The definition of the specific enthalpy density per particle is:

$$\mu = \frac{h}{n} = \frac{n m_p c^2 + \epsilon + p}{n} = m_p c^2 + \frac{\hat{\gamma}}{\hat{\gamma} - 1}\frac{p}{n}, \tag{3.9}$$

where n is the number density of the particles, p is the pressure, c is the light speed, h is the relativistic enthalpy density of the gas, ϵ is the internal energy density, $\hat{\gamma}$ is

the adiabatic index and m_p is the proton mass. Using the conservation equations, the three Taub Adiabats conditions for a relativistic shock can be written in the rest frame of the shock as (e.g., Zhang, 2018)

$$n_1 u_{1s} = n_2 u_{2s}, \tag{3.10}$$

$$\gamma_{1s}\mu_1 = \gamma_{2s}\mu_2, \tag{3.11}$$

$$\mu_1 u_{1s} + \frac{p_1}{n_1 u_{1s}} = \mu_2 u_{2s} + \frac{p_2}{n_2 u_{2s}}, \tag{3.12}$$

where u_{1s} stands for the relative component dimensionless 4-speed between the upstream and the shock front, u_{2s} stands for the relative component dimensionless 4-speed between the downstream and the shock front, γ_{1s} stands for the relative Lorentz factor between the upstream and the shock front, γ_{2s} stands for the relative Lorentz factor between the downstream and the shock front, and γ_{21} stands for the relative Lorentz factor between the upstream and downstream. These quantities can be defined using the relativistic addition of velocities (e.g., Zhang, 2018):

$$u_{1s} = \gamma_{2s}\gamma_{21}(\beta_{2s} + \beta_{21}), \tag{3.13}$$

$$u_{2s} = \gamma_{1s}\gamma_{21}(\beta_{1s} - \beta_{21}), \tag{3.14}$$

$$\gamma_{2s} = \gamma_{1s}\gamma_{21}(1 - \beta_{1s}\beta_{21}), \tag{3.15}$$

$$\gamma_{1s} = \gamma_{2s}\gamma 21(1 + \beta_{2s}\beta_{21}), \tag{3.16}$$

$$\gamma_{21} = \gamma_{1s}\gamma_{2s}(1 - \beta_{1s}\beta_{2s}), \tag{3.17}$$

$$\beta_{2s} = \frac{\beta_{1s} - \beta_{21}}{1 - \beta_{1s}\beta_{21}}, \tag{3.18}$$

$$\beta_{1s} = \frac{\beta_{2s} + \beta_{21}}{1 + \beta_{2s}\beta_{21}}, \tag{3.19}$$

$$\beta_{21} = \frac{\beta_{1s} - \beta_{2s}}{1 - \beta_{1s}\beta_{2s}}. \tag{3.20}$$

3.4 Cold Upstream Fluid

To describe the dynamics of GRBs, the cold upstream fluid assumption is widely used (e.g., Blandford and McKee, 1976). One can use the Taub Adiabats jump equations

(eqs. 3.10-3.12) to find the jump conditions for a cold upstream fluid. It is assumed that $\epsilon_1 = p_1 = 0$, $\mu_1 = m_p c^2$. One can use this solution in the afterglow problem, because the assumed conditions imply that the unshocked upstream is cold. These assumptions lead us to the equations:

$$u_{2s}^2 = \frac{(\gamma_{21}-1)(\hat{\gamma}-1)^2}{\hat{\gamma}(2-\hat{\gamma})(\gamma_{21}-1)+2}, \tag{3.21}$$

$$u_{1s}^2 = \frac{(\gamma_{21}-1)(\hat{\gamma}\gamma_{21}+1)^2}{\hat{\gamma}(2-\hat{\gamma})(\gamma_{21}-1)+2}, \tag{3.22}$$

$$\frac{\epsilon_2}{n_2} = (\gamma_{21}-1)m_p c^2, \tag{3.23}$$

$$\frac{n_2}{n_1} = \frac{\hat{\gamma}\gamma_{21}+1}{\hat{\gamma}-1}, \tag{3.24}$$

$$\gamma_{1s}^2 = \frac{(\gamma_{21}+1)[\hat{\gamma}(\gamma_{21}-1)+1]^2}{\hat{\gamma}(2-\hat{\gamma})(\gamma_{21}-1)+2}. \tag{3.25}$$

In particular, assuming the Lorentz factor is $\gamma_{21} \gg 1$, the shocks are strong. Applying this assumption to the equations 3.7 and 3.21-3.25, one has

$$\hat{\gamma} = \frac{4\gamma_{21}+1}{3\gamma_{21}}, \tag{3.26}$$

$$\frac{\epsilon_2}{n_2} = (\gamma_{21}-1)m_p c^2 \approx \gamma_{21} m_p c^2, \tag{3.27}$$

$$\frac{n_2}{n_1} = 4\gamma_{21}, \tag{3.28}$$

$$u_{1s} \approx \gamma_{1s} \approx \sqrt{2}\gamma_{21}, \quad \beta_{1s} \approx 1, \tag{3.29}$$

$$u_{2s} \approx \frac{\sqrt{2}}{4}, \quad \beta_{2s} \approx \frac{1}{3}, \quad \gamma_{2s} \approx \frac{3}{4}\sqrt{2}, \tag{3.30}$$

one can conclude that a relativistic shock is much stronger than a non-relativistic shock, because the compression ratio for a strong non-relativistic shock is 4 and as one can be seen in the equation 3.28 the compression factor is $4\gamma_{21}$ and, the downstream fluid has a temperature (in the equation 3.27) of the order of $\gamma_{21} m_p c^2$, for a more detailed explanation see Zhang (2018). We can obtain an expression for the downstream internal energy density by combining equations 3.27 and 3.28

$$\epsilon_2 = 4\gamma_{21}(\gamma_{21}-1)n_1 m_p c^2 \approx 4\gamma_{21}^2 n_1 m_p c^2. \tag{3.31}$$

Thus, the internal energy density is approximately $4\gamma_{21}^2$ times the upstream rest mass energy density.

3.5 Shock parameterization

The afterglow shocks are well explained by the acceleration of the electrons in the collisionless relativistic shock waves propelled through the explosion in the circumburts medium (e.g., Waxman, 2006; Zhang, 2018; Gill and Granot, 2022). There are three main processes that occur in collisionless relativistic shocks, as understood using the diffusive shock acceleration theory (e.g., Drury, 1983):
(1) **Particle acceleration**: Particles are accelerated to a power-law energy distribution beyond a certain minimum energy.
(2) **Amplification of the magnetic field**: Small seed B-fields in the upstream fluid are amplified by microscopic (e.g., Medvedev and Loeb, 1999) and macroscopic MHD instabilities (e.g., Sironi and Goodman, 2007) in the downstream fluid.
(3) **Photon radiation**: Shock accelerated particles radiate a part of their energy over the dynamical time mainly via synchrotron and, possibly, inverse-Compton radiative processes.

For a full understanding of the physics of relativistic shocks, very detailed large-scale numerical simulations are required, but as one can imagine, these simulations are very computationally expensive. The simplest solution to this computational problem is to parameterize the shocks with some empirical parameters. The use of these parameters reflects the poor understanding that one has of detailed microscopic physics at the plasma level, but fortunately they make a direct connection to the observational properties. Using these parameters one can greatly reduce the complexity of the phenomenon being studied, in addition to giving a connection between the macroscopic and microscopic worlds. The various shock microphysics parameters are

- p: the power-law index of the non-thermal electrons, defined by $N(E)dE \propto E^{-p}dE$, or $N(\gamma)d\gamma \propto \gamma^{-p}d\gamma$. Similarly, an index for the non-thermal protons, p_p, may also be defined.

- ϵ_B: the fraction of the shock internal energy that is deposited in the magnetic fields.
- ϵ_e: the fraction of the shock internal energy that is deposited in the electrons.
- ϵ_p: the fraction of the shock internal energy that is deposited in the protons.
- ξ_e: the fraction of the shocked electrons that are accelerated to a non-thermal distribution.
- ξ_p: the fraction of the shocked protons that are accelerated to a non-thermal distribution.

By energy conservation one has

$$\epsilon_p + \epsilon_e + \epsilon_B = 1. \tag{3.32}$$

For the GRB afterglow problem, usually $\xi_e = \xi_p = 1$ is assumed to model the forward shock (e.g., Zhang, 2018). However, Eichler and Waxman (2005) found that the afterglow model is degenerate due to the freedom in the value of the parameter $m_e/m_p \leq \xi_e \leq 1$. They showed that the model parameters $(E, n, \epsilon_e, \epsilon_B) = (E^*\xi_e^{-1}, n^*\xi_e^{-1}, \epsilon_e^*\xi_e, \epsilon_B^*\xi_e)$, where $(E^*, n^*, \epsilon_e^*, \epsilon_B^*)$ are the parameters when $\xi_e = 1$, produce exactly the same afterglow solution.

4 Radiative processes

In this chapter I am going to present a brief description of some radiative processes that occur in GRBs. It is known that there are many physical processes involved and I do not seek to exhaustively cover all physical processes in this chapter, these are explained in detail in the following books Rybicki and Lightman (1991); Zhang (2018). In this chapter I will describe some processes that are important to this work like, synchrotron radiation and synchrotron self-Compton (SSC).

4.1 Synchrotron Radiation

Synchrotron radiation is produced by relativistic particles accelerated by a magnetic field. When the speed is not relativistic, this physical process is called cyclotron radiation. This process is important in GRB physics, as it is believed to produce the afterglow and is the leading radiation mechanism candidate for GRB prompt emission. In the following subtopics I will add only the physical results needed to calculate the observed synchrotron spectrum.

4.1.1 Emission in a Magnetic Field

The simplest case is when a charged particle is rotating in a uniform magnetic field with an angle of incidence α (the pitch angle) with respect to the field line emits a synchrotron spectrum in the form of (e.g., Rybicki and Lightman, 1991)

$$P(\nu,\gamma) = \frac{\sqrt{3}q^3 B\sin\alpha}{mc^2} F\left(\frac{\nu}{\nu_{\rm ch}}\right), \tag{4.1}$$

where q is the charge of the particle, m is the mass of the particle, B is a magnetic field, c is the speed of light, γ is the Lorentz factor, ν is frequency, $P(\nu,\gamma) = dE/(dtd\nu)$ is the emitted power per unit frequency, and $\nu_{\rm ch}$ is the characteristic emission frequency

$$\nu_{\rm ch} = \frac{3}{4\pi}\gamma^2\frac{qB_\perp}{mc}, \tag{4.2}$$

where $B_\perp = B\sin\alpha$. The function F is defined by

$$F(x) = x\int_x^\infty K_{5/3}(\xi)d\xi, \tag{4.3}$$

where $x = \nu/\nu_{\rm ch}$, and this function reaches its maximum at $F_{\rm max}(0.29) \approx 0.92$, $K_{5/3}$ is a modified Bessel function, and has the asymptotic behavior

$$F(x) \sim \begin{cases} \frac{4\pi}{\sqrt{3}\Gamma(1/3)}\left(\frac{x}{2}\right)^{1/3} \sim 2.15x^{1/3} & \text{for} \quad x \ll 1, \\ \\ \left(\frac{\pi}{2}\right)^{1/2} e^{-x} \sim 1.25x^{1/2}e^{-x} & \text{for} \quad x \gg 1, \end{cases} \tag{4.4}$$

where $\Gamma(1/3)$ is the gamma function. So the synchrotron spectrum for individual particles, P, has a $\propto \nu^{1/3}$ behavior at low energies and an exponential cutoff at high energies. The total emission power of the particle is

$$P(\gamma) = 2\sigma_T c\gamma^2\beta_\perp^2 U_B, \tag{4.5}$$

where $\beta_\perp = v\sin\alpha/c$ is the dimensionless perpendicular velocity of the particle, $U_B = B^2/8\pi$ is the magnetic field energy density in the emission region, and $\sigma_T \approx 6.65 \times 10^{-25}$ cm^2 is the electron Thomson cross section. Nevertheless, in practice there is not emission of a single particle, so it is necessary to know the equation for a collection of particles in a uniform magnetic field.

The observed emission from astrophysical sources comes from a population of particles emitting in a magnetic field whose configuration is unknown. Therefore, the observed

spectrum depends on the energy distribution of the particles and the configuration of the magnetic field. As mentioned above, the energy distribution of particles is assumed to follow a power-law, i.e.

$$N(\gamma)d\gamma = C_\gamma \gamma^{-p} d\gamma, \quad \gamma_m < \gamma < \gamma_M, \tag{4.6}$$

this is a power-law distribution of the particle energy with an energy spectral index p in terms of the Lorentz factor of relativistic particles. Here γ_M and γ_m are the maximum and minimum Lorentz factors of the electron energy distribution, respectively and $C_\gamma = C_E(m_e c^2)^{1-p}$. Where C_γ and C_E are normalization constants related to particle distributions in terms of energy ($N(E)$) or in terms of the Lorentz factor ($N(\gamma)$). If one integrates the synchrotron spectra of individual particles over the energy distribution of the particles in the range $\nu_m < \nu < \nu_M$, one gets the observed spectrum of a set of particles with a power-law distribution

$$F_\nu = \int_{\gamma_m}^{\gamma_M} P(\nu,\gamma) C_\gamma \gamma^{-p} d\gamma \propto \nu^{-\frac{p-1}{2}}, \tag{4.7}$$

this is the simplest case, with a uniform magnetic field and a constant pitch angle for all the electrons. After some intermediate steps one has as a result, for a population of electrons with a power-law distribution defined by their minimum and maximum Lorentz factors γ_m and γ_M, the synchrotron radiation spectrum has three segments

$$F_\nu \propto \begin{cases} \nu^{1/3} & \text{for} \quad \nu < \nu_m = \frac{3}{4\pi}\gamma_m^2 \frac{eB_\perp}{m_e c}, \\ \nu^{-(p-1)/2} & \text{for} \quad \nu_m < \nu < \nu_M = \frac{3}{4\pi}\gamma_M^2 \frac{eB_\perp}{m_e c}, \\ \nu^{1/2} e^{-(\nu/\nu_M)} & \text{for} \quad \nu > \nu_M. \end{cases} \tag{4.8}$$

In collisionless relativistic shocks (e.g., Moiseev and Sagdeev, 1963; Benz, 2012), that give rise to the afterglow, and may even produce the prompt emission, the magnetic field is produced on small scales (e.g., Medvedev and Loeb, 1999; Sironi and Spitkovsky, 2009) with angular coherence length $\theta_B \ll 1/\Gamma$, where $1/\Gamma$ is the angular size of the observable part of the jet in GRBs and, Γ is the bulk Lorentz factor. In addition, this magnetic field is not ordered but instead it is tangled up and randomly oriented. So now one needs to know the equations averaged over the directions of the random magnetic field, which effectively is an average over the pitch angles of the particles. The synchrotron emission power of a single particle with the pitch angle of Eq. 4.5 averaged over the angles $\langle \beta_\perp^2 \rangle = 2\beta^2/3$ is

$$P(\gamma) = \frac{4}{3}\sigma_T c \gamma^2 \beta^2 U_B. \tag{4.9}$$

In a random B field the trajectory of the charged particle does not keep a constant angle α with respect to the magnetic field as in the uniform B case. An important condition for the synchrotron emission is if the particle gyrates enough to cause its relativistic beam to sweep an angle much greater than $1/\gamma$. The relevant parameter (e.g., Medvedev, 2000) is the ratio between the "particle deflection angle" and the angular size of the emission beam $1/\gamma$, i.e.

$$\delta = \gamma \frac{\lambda_B}{r_B}, \tag{4.10}$$

where λ_B is the relationship between the typical correlation scale of random magnetic fields, and $r_B = \gamma m_e c^2 / e B_\perp$ is the Larmor radius. When $\delta \gg 1$, the spectrum of an ensemble of particles with a power-law distribution is given by equation 4.8, but $B_\perp$ replaced by the averaged magnetic field, i.e., one has to replace $B_\perp$ by B.

4.1.2 Synchrotron Cooling

During the propagation of a relativistic shock new energetic particles are constantly accelerated at the shock front and these particles lose energy (or cool) through various radiation mechanisms. To calculate the time-dependent synchrotron emission spectrum from the system, the electron energy distribution as a function of time has to be solved self-consistent by properly considering injection of new particles, cooling, and heating of old ones.

The synchrotron cooling time of a relativistic particle with energy γmc^2 and a synchrotron power given by eq. 4.9 with a magnetic energy density $U_B = B^2/8\pi$ can be written as (e.g., Zhang, 2018)

$$\tau(\gamma) = \frac{6\pi m_e c}{\gamma \sigma_T \beta^2 B^2}. \tag{4.11}$$

After the acceleration of a set of particles with a power law distribution, the cooling energy or cooling Lorentz factor of the particles above which the particles have lost most of their energies is defined by $t = \tau(\gamma_c)$, where γ_c is

$$\gamma_c(t) \approx \frac{6\pi m_e c}{\sigma_T B^2 t}, \tag{4.12}$$

where $\beta \sim 1$, because the particles that produce synchrotron radiation are relativistic with $\gamma \gg 1$. Since electrons are continuously being injected into the system while also being cooled, the system at any given time will have electrons with different "ages", adding a new part to the power-law of the synchrotron spectrum, defined by the cooling frequency ν_c.

If we neglect the spatial distributions of the particles, the temporal evolution of the particles in energy space for an open system of particles (that is, a system where there is an exchange of information, energy or mass between the system and its environment) takes the form of the Fokker-Planck equation (e.g., Chandrasekhar,

1943), where, the equation of continuity in the energy space simplifies to

$$\frac{\partial N(\gamma,t)}{\partial t} = -\frac{\partial}{\partial \gamma}\left[\dot{\gamma}(\gamma) N(\gamma,t)\right] + Q(\gamma,t), \tag{4.13}$$

where, $N(\gamma,t)$ is the particle number within the energy interval $(\gamma, \gamma + d\gamma)$ at time t, $\dot{\gamma}(\gamma)$ is the energy gain rate of the particles with energy γ, and $Q(\gamma,t)$ is the source term, denoting the energy-dependent injection rate of particles into the system.
In a system with continuous cooling and injection of fresh particles assuming $Q(\gamma) \propto \gamma^{-p}$ for $\gamma_m < \gamma < \gamma_M$, its particle energy distribution at any epoch t scales as:

$$N(\gamma,t) \propto \begin{cases} \gamma^{-p} & \text{for} \quad \gamma_m < \gamma < \gamma_c < \gamma_M, \\ \\ \gamma^{-(p+1)} & \text{for} \quad \gamma_m < \gamma_c < \gamma < \gamma_M, \end{cases} \tag{4.14}$$

The cooled distribution is steeper by one power compared to the uncooled distribution. For the slow cooling regime ($\gamma_m < \gamma_c$), and

$$N(\gamma,t) \propto \begin{cases} \gamma^{-2} & \text{for} \quad \gamma_c < \gamma < \gamma_m < \gamma_M, \\ \\ \gamma^{-(p+1)} & \text{for} \quad \gamma_c < \gamma_m < \gamma < \gamma_M, \end{cases} \tag{4.15}$$

for the fast cooling regime ($\gamma_c < \gamma_m$), where γ_m, γ_c and γ_M are instantaneous values of the minimum injection, cooling and maximum injection energies of the electrons at time t. This applies to any cooling mechanism that has $\dot{\gamma} \propto \gamma^2$, which is the case for synchrotron radiation and also for inverse Compton scattering. Since the emitted spectrum takes the form $F_\nu \propto \nu^{-(p-1)/2}$ when the radiating electron distribution is $N(\gamma) \propto \gamma^{-p}$, $d\ln F_\nu / d\ln \nu$ changes as the power-law index $d\ln N(\gamma)/d\ln\gamma$ changes in

a given power-law segment of the particle distribution.

$$F_\nu \propto \begin{cases} \nu^{1/3} & \text{for} \quad \nu < \nu_m, \\ \nu^{-(p-1)/2} & \text{for} \quad \nu_m < \nu < \nu_c < \nu_M, \\ \nu^{-p/2} & \text{for} \quad \nu_m < \nu_c < \nu < \nu_M, \end{cases} \tag{4.16}$$

for slow cooling, and

$$F_\nu \propto \begin{cases} \nu^{1/3} & \text{for} \quad \nu < \nu_c, \\ \nu^{-1/2} & \text{for} \quad \nu_c < \nu < \nu_m < \nu_M, \\ \nu^{-p/2} & \text{for} \quad \nu_c < \nu_m < \nu < \nu_M, \end{cases} \tag{4.17}$$

for fast cooling, where ν_m, ν_c and ν_M are the corresponding characteristic synchrotron emission frequencies for the electrons with Lorentz factors γ_m, γ_c and γ_M, respectively.

4.1.3 Synchrotron Self-Absorption

The synchrotron emission is also accompanied by absorption, that is, when a photon interacts with a charge in a magnetic field and is absorbed, giving up its energy to the charge. This happen in the optically thick region at low frequencies and produces a low-frequency cutoff of the spectrum (e.g., Rybicki and Lightman, 1991). For an optically thick medium, with optical depth to absorption $\tau_\nu \gg 1$, the radiation transfer equation takes the form

$$F_\nu \propto S_\nu = \frac{j_\nu}{\alpha_\nu}, \tag{4.18}$$

where α_ν is the absorption coefficient and j_ν is the emission coefficient, and S_ν the source function (e.g., Rybicki and Lightman, 1991). First, the absorption coefficient for a power-law distribution of electrons (Eq.4.6) and for standard synchrotron radiation (Eq.4.1) is defined by

$$\alpha_\nu = \frac{(p+2)}{8\pi m_e} C_\gamma \nu^{-2} \int_{\gamma_m}^{\gamma_M} \frac{\sqrt{3} e^3 B_\perp}{m_e c^2} F(x) \gamma^{-(p+1)} d\gamma, \tag{4.19}$$

The emission coefficient is defined by (Rybicki and Lightman, 1991)

$$j_\nu = \left(\frac{1}{4\pi}\right) \int_{\gamma_m}^{\gamma_M} P(\gamma, \nu) N(\gamma) d\gamma. \tag{4.20}$$

Finally, if one integrates the Eq.4.19 and Eq.4.20, one can find the spectral indices in the synchrotron self-absorbed regime

$$F_\nu \propto S_\nu \propto \begin{cases} \frac{\nu^{-(p-1)/2}}{\nu^{-(p+4)/2}} \propto \nu^{5/2} & \text{for} \quad \gamma_m \ll \gamma(\nu) \ll \gamma_M, \\ \\ \frac{\nu^{1/3}}{\nu^{-5/3}} \propto \nu^2 & \text{for} \quad \gamma(\nu) \ll \gamma_m < \gamma_M. \end{cases} \tag{4.21}$$

The frequency below which the synchrotron flux self-absorbs is called the self-absorption frequency ν_a, and there are two main methods to calculate it: (1) the optical depth method: this method assumes that all the electrons are associated with protons and that all electrons are accelerated, (see in detail Zhang, 2018); (2) the Blackbody method: this method consists of equating the Rayleigh-Jeans spectrum to the synchrotron spectrum. The latter method is the most widely used in the literature (e.g. Piran et al., 1999). The advantages of this method are that, in most cases, some parameters can be derived directly from observations, so the result does not depend on unknown details.

4.1.4 Broken Power-Law Spectra

To model the spectrum of synchrotron radiation under the effects of cooling and self-absorption, one can use a broken power-law spectrum. Using the eq.4.1 one can find the average of the maximum specific emission power of an individual electron in the observer's frame of reference (e.g., Wijers and Galama, 1999):

$$P_{\nu,\max} = \frac{\sqrt{3}\phi e^3}{m_e c^2} B\Gamma, \tag{4.22}$$

where ϕ is the maximum flux in equation 4.3, and Γ is the bulk Lorentz factor. Analyzing the equation 4.22, one notices that it does not depend on the γ of the electrons, because this is the maximum power per unit frequency that can be emitted for a given magnetic field. The maximum flux density is:

$$F_{\nu,\max} = (1+z)\frac{N_{\rm tot} P_{\nu,\max}}{4\pi D_L^2}, \tag{4.23}$$

where $N_{\rm tot}$ is the total number of electrons, z is the cosmological redshift of the burst and D_L is the luminosity distance of the burst. In total one has three characteristic frequencies ν_a, ν_m and ν_c for the synchrotron spectrum. There are two ways to classify the regime of each case. When $\nu_a < \nu_c$ is for weak absorption and $\nu_a > \nu_c$ is for strong absorption, but this form is not widely used for GRB phenomena because ν_a is not

large enough to enter a strong absorption regime. The equations for these cases can be written as :

In the case of slow cooling, weak absorption (see Figure 4.1):

$$F_\nu = F_{\nu,\max} \begin{cases} \left(\frac{\nu_a}{\nu_m}\right)^{1/3} \left(\frac{\nu}{\nu_a}\right)^2 & \text{for} \quad \nu < \nu_a, \\ \left(\frac{\nu}{\nu_m}\right)^{1/3} & \text{for} \quad \nu_a < \nu < \nu_m, \\ \left(\frac{\nu}{\nu_m}\right)^{-\frac{p-1}{2}} & \text{for} \quad \nu_m < \nu < \nu_c, \\ \left(\frac{\nu_c}{\nu_m}\right)^{-\frac{p-1}{2}} \left(\frac{\nu}{\nu_c}\right)^{-p/2} & \text{for} \quad \nu_c < \nu < \nu_M. \end{cases} \tag{4.24}$$

In the case of fast cooling, weak absorption (see Figure 4.2):

$$F_\nu = F_{\nu,\max} \begin{cases} \left(\frac{\nu_a}{\nu_c}\right)^{1/3} \left(\frac{\nu}{\nu_a}\right)^2 & \text{for} \quad \nu < \nu_a, \\ \left(\frac{\nu}{\nu_c}\right)^{1/3} & \text{for} \quad \nu_m < \nu < \nu_c, \\ \left(\frac{\nu}{\nu_c}\right)^{-\frac{1}{2}} & \text{for} \quad \nu_c < \nu < \nu_m, \\ \left(\frac{\nu_m}{\nu_c}\right)^{-\frac{1}{2}} \left(\frac{\nu}{\nu_m}\right)^{-p/2} & \text{for} \quad \nu_m < \nu < \nu_M. \end{cases} \tag{4.25}$$

These spectra were published by Sari et al. (1998) and for illustration, see Figure 4.1 for slow cooling and Figure 4.2 for fast cooling.

The expressions for the break frequencies and the peak flux of the synchrotron spectrum are (for $p = 2.2$):

$$\nu_a^{\rm slow} = 3.6{\rm GHz}(1+z)^{-1}\epsilon_{e,0.5}^{-1}\epsilon_{B,-2}^{1/5}E_{52}^{1/5}n_1^{3/5}, \tag{4.26}$$

$$\nu_a^{\rm fast} = 0.15{\rm GHz}(1+z)^{-1/2}\epsilon_{B,-2}^{6/5}E_{52}^{7/10}n_1^{11/10}t_{\rm day}^{-1/2}(1+Y), \tag{4.27}$$

$$\nu_m = 5\times10^{12}{\rm Hz}(1+z)^{1/2}\epsilon_{B,-2}^{1/2}\epsilon_{e,0.5}^{2}E_{52}^{1/2}t_{day}^{-3/2}, \tag{4.28}$$

$$\nu_c = 2.7\times10^{15}{\rm Hz}(1+z)^{-1/2}\epsilon_{B,-2}^{-3/2}E_{52}^{-1/2}n_1^{-1}t_{day}^{-1/2}(1+Y)^{-2}, \tag{4.29}$$

$$F_{\nu,\rm max} = 2.6{\rm mJy}(1+z)\epsilon_{B,-2}^{1/2}E_{52}n_1^{1/2}D_{L,28}^{-2}, \tag{4.30}$$

where $n = n_1 \times 1$ cm^{-3} is the density of the external medium, $E = E_{52}\times10^{52}$ ergs s^{-1} is the total energy of the explosion, $D_L = D_{L,28}\times10^{28}$ cm is the luminosity distance and, $\epsilon_B = \epsilon_{B,-2}\times10^{-2}$ and $\epsilon_e = \epsilon_{e,0.5}\times0.5$ are the fractions of the internal energy of the shock deposited in magnetic fields and electrons, respectively.

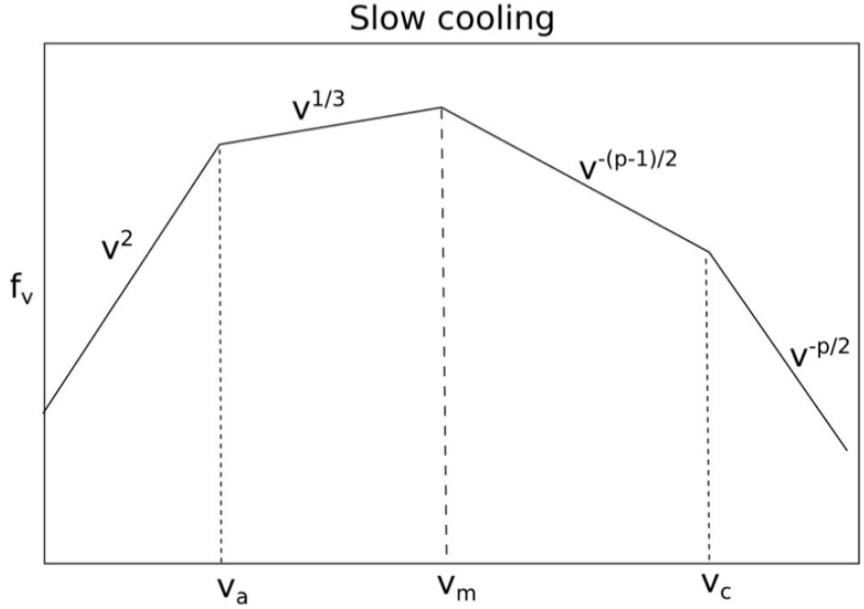

Figure 4.1: Synchrotron spectrum in slow cooling regime for a power-law electron distribution (Figure 1b of Sari et al. (1998))

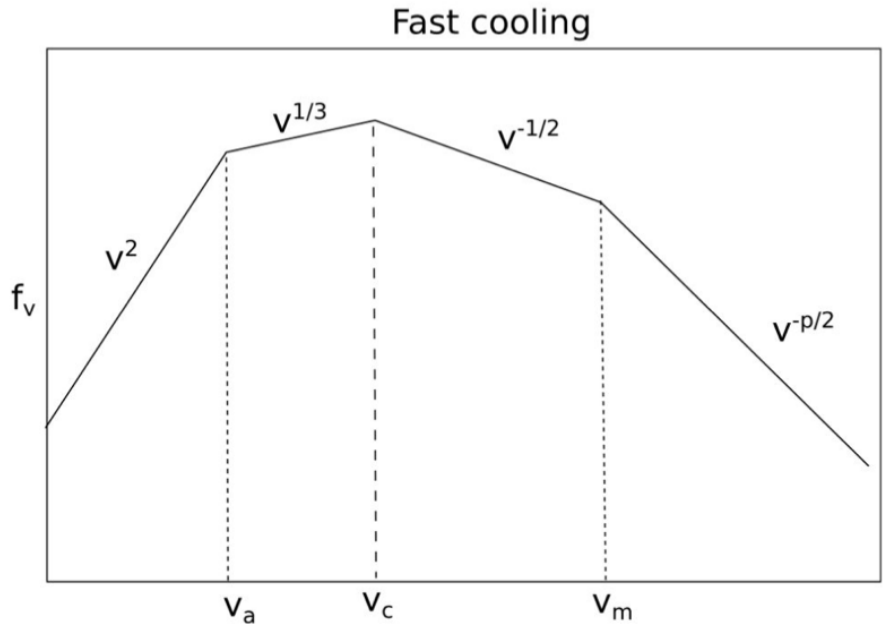

Figure 4.2: Synchrotron spectrum in fast cooling regime for a power-law electron distribution (Figure 1a of Sari et al. (1998))

4.2 Synchrotron Self-Compton (SSC)

Another important radiation process in GRBs is inverse Compton scattering. Compton scattering and inverse Compton scattering will be explained briefly for more details, see (e.g., Rybicki and Lightman, 1991; Zhang, 2018). The easiest way to understand Compton scattering is to imagine that a free electron and an incident photon (incident on the free electron), after the photon interacts with the electron it is scattered in a certain direction with a loss of energy when the scattering is incoherent or inelastic. In inverse Compton scattering (IC) the process is the same except that the photon is scattered incoherently from a moving electron, and the scattered photon gains more energy, this energy is subtracted from the energy of the electron. There are two important regimes in Compton scattering, these are determined by the energy of the incident photon with respect to the rest mass energy of the electron. The Compton scattering cross section is (e.g., Rybicki and Lightman, 1991)

$$\sigma = \frac{3}{4}\sigma_T \left[\frac{1+x}{x^3} \left(\frac{2x(1+x)}{1+2x} - \ln(1+2x) \right) + \frac{1}{2x}\ln(1+2x) - \frac{1+3x}{(1+2x)^2} \right], \quad (4.31)$$

and this cross section can be simplified for Thomson ($x \ll 1$) and Klein-Nishina ($x \gg 1$) regimes as:

$$\sigma = \begin{cases} \sigma_T(1 - 2x + \frac{26}{5}x^2 + ...) & \text{for} \quad x \ll 1, \\ \\ \frac{3}{8}\sigma_T x^{-1}(\ln 2x + \frac{1}{2}) & \text{for} \quad x \gg 1, \end{cases} \tag{4.32}$$

where

$$x = \frac{h\nu}{m_e c^2}. \tag{4.33}$$

For $x \ll 1$, one has the Thomson regime, where the cross section is $\sim \sigma_T$. For $x \gg 1$, one has the Klein-Nishina (KN) regime. The cross section σ in the KN regime is suppressed, that is, if the equation 4.32 is observed, there is a σ_T/x term that makes the scattering cross section smaller, so scattering will be less effective.

In the Thomson regime, the equation for the IC emission power of a single electron is almost the same that the synchrotron power of a single particle. The difference is only the energy density, i.e.

$$P_{IC} \approx \frac{4}{3}\sigma_T c(\gamma\beta)^2 U_{ph}, \tag{4.34}$$

where U_{ph} is the energy density of the target photons. Thus, combining the equation 4.9 with the equation 4.34 one has the Y parameter

$$Y = \frac{P_{IC}}{P_{syn}} \approx \frac{U_{ph}}{U_B}. \tag{4.35}$$

The energy density determines which mechanism is the one that dominates the cooling of the electrons.

When the synchrotron photons radiated by the electrons suffer inverse Compton scattering by the same distribution of electrons is called synchrotron self-Compton (SSC),

in addition to presenting a higher efficiency for the loss of energy of the electrons than synchrotron alone. Since this process can be repeated several times, one can write the total power emitted by the electrons as

$$P_{tot} = P_{syn} + P_{SSC,1} + P_{SSC,2} + ...+, \tag{4.36}$$

where $P_{SSC,1} = (4/3)\gamma^2\sigma_T c\beta^2 U_B Y_1$, $P_{SSC,2} = (4/3)\gamma^2\sigma_T c\beta^2 U_B Y_1 Y_2$ (e.g., Zhang, 2018), rewriting equation 4.36

$$P_{tot} = P_{syn}(1 + Y_1 + Y_1 Y_2 + ...). \tag{4.37}$$

The introduction of SSC results in an enhanced cooling. When the Klein-Nishina correction is not important, we have $Y_1 = Y_2 = ... = Y$ (e.g., Barniol Duran et al., 2012; Zhang, 2018), because a first-order SSC power that is Y times the synchrotron power is going to produce a SSC power energy density that also Y times that of the synchrotron.

Usually for GRBs the second-order SSC term is not important (e.g., Resmi and Zhang, 2012; Nakar et al., 2009) and, one can write the total emission power as

$$P_{tot} = P_{syn}(1 + Y). \tag{4.38}$$

The Y parameter will connect the microphysical parameters of the shock with the SSC processes. In particular, Sari and Esin (2001) give a simple way to write this parameter:

$$Y = \frac{U_{syn}}{U_B} = \frac{\eta_e \epsilon_e}{\epsilon_B(1 + Y)}, \tag{4.39}$$

where

$$\eta_e = \begin{cases} 1 & \text{for} \quad \text{fast cooling}, \\ \\ \left(\frac{\gamma_c}{\gamma_m}\right)^{2-p} & \text{for} \quad \text{slow cooling}, \end{cases} \tag{4.40}$$

is the electron radiation efficiency. Solving the eq. 4.39 for Y, we will get

$$Y = \begin{cases} \frac{\eta_e \epsilon_e}{\epsilon_B} & \text{for} \quad \frac{\eta_e \epsilon_e}{\epsilon_B} \ll 1, \\ \\ \left(\frac{\eta_e \epsilon_e}{\epsilon_B}\right)^{1/2} & \text{for} \quad \frac{\eta_e \epsilon_e}{\epsilon_B} \gg 1. \end{cases} \tag{4.41}$$

The IC flux is strongly related to the synchrotron flux. The observed IC flux is defined as (e.g., Sari and Esin, 2001):

$$F_\nu^{IC} = \Delta' \sigma_T \int_{\gamma_m}^{\infty} d\gamma N(\gamma) \int_0^{x_0} dx F_\nu(x), \tag{4.42}$$

where Δ' is the comoving size of the emission region, x_0 is a value introduced to ensure energy conservation, and $F_\nu(x)$ is the specific synchrotron flux. We can write the analytical approximations of the IC flux as the equations 4.25-4.24, and the spectrum looks like Figure 4.3. The shape of the approximate analytical SSC spectra is similar to the shape of the synchrotron spectra because the SSC spectra are the convolution of the electron distribution times the synchrotron flux. The critical frequencies observed in the Figure 4.3 are (e.g., Sari and Esin, 2001) :

$$\nu_a^{IC} = 2\gamma_m^2 \nu_a, \tag{4.43}$$

$$\nu_c^{IC} = 2\gamma_c^2 \nu_c, \tag{4.44}$$

$$\nu_m^{IC} = 2\gamma_m^2 \nu_m. \tag{4.45}$$

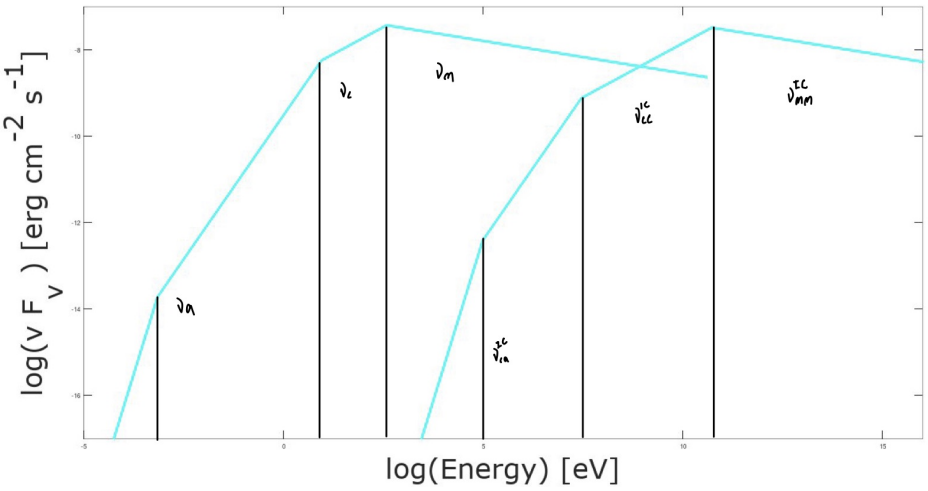

Figure 4.3: Example of synchrotron (left) and SSC (right) spectrum. The regime is fast cooling.

If one wants a more accurate SSC spectra, the numerical simulations are necessary to take a more general treatment of the IC flux.

4.3 Pair Production

When photons have high enough energy ($\geq 2m_e c^2$), pair production can occur. The main idea of the pair production is that when one has a high energy neutral boson, this boson will create a subatomic particle and its antiparticle, and generally this process is followed by the reverse process (pair annihilation) (e.g., Zhang, 2018). The main process in GRBs are the so-called two-photon pair production ($\gamma\gamma \longrightarrow e^+e^-$) process see Figure 4.4. As one knows from the theory of relativity that quantity:

$$E^2 - |\mathbf{p}|^2c^2 = m_e^2c^4\gamma^2(1-\beta^2) = m_e^2c^4 = const, \tag{4.46}$$

is an invariant. So if one takes two photons (i.e. $\gamma_1\gamma_2 \longrightarrow e^+e^-$), we have:

$$(E_{\gamma,1} + E_{\gamma,2})^2 - (\mathbf{p}_{\gamma,1} + \mathbf{p}_{\gamma,2})^2c^2 = (E_{e^+} + E_{e^-})^2 - (\mathbf{p}_{e^+} + \mathbf{p}_{e^-})^2c^2. \tag{4.47}$$

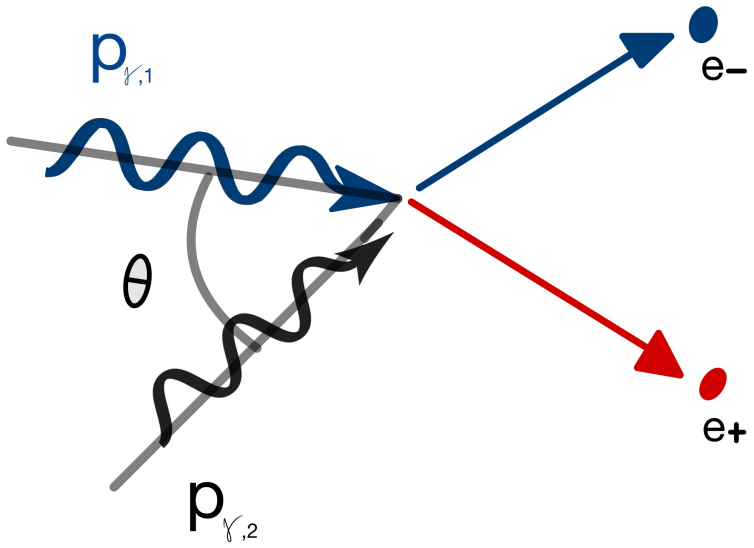

Figure 4.4: Two-photons pair production.

When $E_{e^+} = E_{e^-} = E$, $\mathbf{p}_{e^+} = \mathbf{p}_{e^-} = \mathbf{p}$, $E_{\gamma,1} = h\nu_1$, and $E_{\gamma,2} = h\nu_2$, the left hand side of the equation 4.47 then becomes

$$2E_{\gamma,1}E_{\gamma,2} - 2\mathbf{p}_{\gamma,1} \cdot \mathbf{p}_{\gamma,2}c^2 = 2h\nu_1 h\nu_2(1 - \cos\theta) \tag{4.48}$$

where θ is the incident angle (see figure 4.4). When one has $\cos\theta = -1$, i.e. a head-on collision, the equation 4.48 gives the threshold condition for two-photon pair production:

$$h\nu_1 \cdot h\nu_2 \geq (m_e c^2)^2. \tag{4.49}$$

5 Afterglow model

In this chapter we will look at the dynamics of the blastwave that produces the afterglow emission. The physics of the afterglow phase is better understood than the prompt emission phase, because blastwaves are also found in other astrophysical sources, like AGN jets and supernovae. In fact, the afterglow emission generally does not need a complete understanding of what is the mechanism by which the relativistic jet is created, that is, if the origin is a merger of compact objects or the collapse of a massive star. In addition to explaining the dynamics, this chapter will summarize the equations of the radiative processes seen in the previous section, particularly the synchrotron process.

5.1 Dynamics in the Self-Similar Regime

The physics of the reverse shock will not be taken into account in this analysis. Consider a blastwave that begins to decelerate. The deceleration is due to mass accumulating as the jet moves through the external medium. When this occurs, the blastwave is said to enter a self-similar regime (e.g., van Eerten, 2014). This regime of self-similarity matters because one only has to pay attention to the energy of the blastwave and the density of the medium. The simplest case is when one does not have loss or injection of energy and the medium is the "ISM" medium, that is, one has a constant energy in the blastwave and a constant density of the external medium. One can know how the blastwave evolves in time, how it decelerates and how it grows

(e.g., Mészáros and Rees, 1997; Sari et al., 1998; Zhang, 2018):

$$\Gamma \propto r^{-3/2} \propto t^{-3/8}, \quad r \propto t^{1/4}, \tag{5.1}$$

where Γ is the Lorentz factor of the blastwave, r is the blastwave distance from central engine, and t is the observer time. Now, if one wants to introduce a density profile that is not constant for the medium, one can use (e.g., Zhang, 2018)

$$n = n_0 \left(\frac{r}{r_0}\right)^{-k}, \tag{5.2}$$

where k is called stratification parameter. With this profile, The scalings 5.1 change to (for more details see Zhang (2018); Dermer and Menon (2009))

$$\Gamma \propto r^{\frac{k-3}{2}} \propto t^{\frac{k-3}{8-2k}}, \quad r \propto t^{\frac{1}{4-k}}. \tag{5.3}$$

5.2 Blandford-Mckee Self-Similar Solution

There already exists a self-similar solution that describes the internal structure of a blastwave. This solution was found by Blandford and McKee (1976) and gives a simple functional form of the density, the Lorentz factor and the internal energy density as a function of a spatial coordinate. For an afterglow model, it is more convenient to pay attention to how the shock front radius (R) and the Lorentz factor of the blastwave evolve over time. The energy of the blastwave for this model with a external medium profile $\rho = AR^{-k}$ ($k = 0$ for ISM and, $k = 2$ for stellar wind) is (e.g., Blandford and McKee, 1976; Granot and Sari, 2002):

$$E = \frac{8\pi}{(17 - 4k)} AR^{-2}(c\hat{t})^3[\Gamma_{sh}(\hat{t})]^2, \tag{5.4}$$

where A is a constant of a external medium density profile, and $\hat{t}$ is the lab-frame time. The shock front Lorentz factor and the shock front radius in terms of the

observer time $t = t_z(1+z)$ are (e.g., Blandford and McKee, 1976; Zhang, 2018)

$$R(t_z) = \left(\frac{(17-4k)(4-k)Et_z}{4\pi Ac}\right)^{1/(4-k)}, \tag{5.5}$$

$$\Gamma_{sh}(t_z) = \left(\frac{(17-4k)E}{4^{5-k}(4-k)^{3-k}\pi Ac^{5-k}t_z^{3-k}}\right)^{\frac{1}{2(4-k)}}. \tag{5.6}$$

5.3 Dynamics of a thin shell

Undoubtedly, it is important to consider the radial structure of the downstream flow, as found by Blandford and McKee (1976), and the emission arising from it in the slow cooling regime. Some simplifying assumptions can be made, as done here for simplicity and computational convenience, such as considering only the dynamical evolution of an infinitely thin shell. Here the thin shell approach is used to model the interaction of the shock with the external medium. The lab-frame width of the thin shell is taken to be $\Delta \ll R/\Gamma^2$, where R/Γ^2 is the lab-frame width of the shocked region. The Lorentz factor of the shock is $\Gamma_{\rm sh} = \sqrt{2}\Gamma$ for an ultra-relativistic blast wave (see equation 3.29), where Γ is the the Lorentz factor of the shocked region immediately downstream of the shock. The slight distinction between the two Lorentz factors is usually made since $\Gamma_{\rm sh}$ is used to calculate the dynamics and Γ is used to determine the Lorentz transformation between the comoving and the observer frame quantities. However, in the thin-shell approach the assumption of $\Gamma_{\rm sh} = \Gamma$ is made. Next, we calculate the dynamical evolution of this thin shell which is implemented in the numerical code (see Section 6.1) used in this work.

The shell sweeps away the external medium, and the outflow slows down when the collected mass ($m_{\rm dec}$) is comparable to (e.g., Zhang, 2018)

$$m_{\rm dec} \sim \frac{M_0}{\Gamma_0}, \tag{5.7}$$

where Γ_0 and M_0 are the initial Lorentz factor and mass of the ejecta. We define the deceleration radius with the isotropic equivalent kinetic energy of the blast wave

(e.g., Gill and Granot, 2018a)

$$E_{k,\rm iso} = m(R_{\rm dec})u_0^2 c^2, \tag{5.8}$$

where $m(R) = (4\pi A/(3-k))R^{3-k}$ is the swept-up mass up to radius R, and solving eq. 5.8 for $R_{\rm dec}$ (e.g., Zhang, 2018; Gill and Granot, 2018a) we get

$$R_{\rm dec} = \left[\frac{(3-k)E_{k,\rm iso}}{4\pi A c^2 u_0^2}\right]^{1/(3-k)}, \tag{5.9}$$

where $u_0 = \Gamma_0\beta_0$ is the initial dimensionless proper 4-speed. When $\Gamma_0 \gg 1$ the 4-speed is $u_0 \approx \Gamma_0$ since $\beta_0 \sim 1$, so the equation 5.9 can be rewritten as

$$R_{\rm dec} = \left[\frac{(3-k)E_{k,\rm iso}}{4\pi A c^2 \Gamma_0^2}\right]^{1/(3-k)}. \tag{5.10}$$

For the evolution of the bulk Lorentz factor, we will assume an adiabatic flow, to be able to write the conservation of energy of the original shell of rest mass M_0 and initial kinetic energy $E_0 = (\Gamma_0 - 1)M_0c^2$ equals to the kinetic energy of the blast wave after it has swept up and shocked mass $m(R)$, $E = \Gamma(M_0c^2 + hV) = M_0c^2(\Gamma - 1) + m(R)c^2(\Gamma^2 - 1)$ where h is the enthalpy density in the shocked region (see equation 3.9), and V is the volume of the shell. By defining the dimensionless radius $\chi = R/R_{\rm dec}$, one obtains that $m/M_0 = \chi^{3-k}/(\Gamma_0 + 1)$, and energy conservation gives (e.g. Panaitescu and Kumar, 2000; Gill and Granot, 2018a):

$$\frac{\chi^{3-k}}{\Gamma_0 + 1}(\Gamma^2 - 1) + \Gamma - \Gamma_0 = 0\,. \tag{5.11}$$

Solving for Γ yields

$$\Gamma = \frac{\Gamma_0 + 1}{2}\chi^{k-3}\left[\sqrt{1 + \frac{4\Gamma_0}{\Gamma_0 + 1}\chi^{k-3} + \left(\frac{2\chi^{3-k}}{\Gamma_0 + 1}\right)^2} - 1\right]. \tag{5.12}$$

This expression is very general and can be applied to non-relativistic and relativistic regimes. Now to find the number density of electrons injected into the shock per unit

time in the comoving frame we write

$$\dot{n}'_e = \frac{1}{V'}\frac{dN'}{dt'}, \tag{5.13}$$

where dN'/dt' is the rate of injection of electrons where N' is the number of electrons, $V' = 4\pi R^2 \Delta'$ is the comoving volume of the shell, $\Delta' = R/(4(3-k)\Gamma)$ is the comoving radial width, then the volume of the shell is

$$V' = \frac{\pi R^3}{(3-k)\Gamma}. \tag{5.14}$$

The differential number of electrons entering the shock as it moves an infinitesimal radial distance is

$$dN = dN' = 4\pi R^2 n dR, \tag{5.15}$$

where we have made use of the invariance of the number of electrons, and where $n \propto R^{-k}$ is the density of the upstream medium, and $dR = \beta c dt = \beta c \Gamma dt'$, rewriting eq. (5.15):

$$dN = dN' = 4\pi R^2 n \beta c \Gamma dt'. \tag{5.16}$$

Substituting eq. (5.14) and eq. (5.16) into eq. (5.13)

$$\dot{n}'_e = \frac{4(3-k)n\Gamma^2\beta c}{R}, \tag{5.17}$$

is the number of injected electrons per unit time and volume.

5.4 Afterglow Emission

Now that we have the blastwave dynamics, we can use our favorite radiation mechanism, i.e. synchrotron radiation, for the afterglow and try to couple it to the shock dynamics. To do this, let us remember that the spectrum follows a power law char-

acterized by the frequencies ν_m, ν_c and ν_a (see Chapter 4 for further details). So in this section we will give the necessary forms to do this. The first step is to know the relation of the observed synchrotron frequency with the parameters of the shock dynamics:

$$\nu \approx \frac{3}{4\pi}\Gamma\gamma^2\frac{eB'}{m_e c}, \tag{5.18}$$

where γ is the comoving Lorentz factor of an electron in the shocked region, Γ is the bulk Lorentz factor of the shocked material just behind the shock, and B' is the comoving magnetic field strength.

When we have a shock that somehow only accelerates a fraction ξ_e of the total shocked electrons into a power-law energy distribution, the minimum injection Lorentz factor γ_m of this distribution is defined as:

$$\gamma_m = g(p)\frac{\epsilon_e}{\xi_e}(\Gamma - 1)\frac{m_p}{m_e}\frac{n_p}{n_e}, \tag{5.19}$$

where $g(p)$ is

$$g(p) \approx \begin{cases} \frac{p-2}{p-1} & \text{for} \quad p > 2, \\ \\ \ln^{-1}(\gamma_M/\gamma_{m'}) & \text{for} \quad p = 2, \end{cases} \tag{5.20}$$

where $\gamma_m = g(p)\bar{\gamma}$ is the general form to write γ_m, where $\bar{\gamma}$ is the average Lorentz factor of the electrons, and for equation 5.19 the average Lorentz factor of the electrons with $n_p = n_e$ (unless the upstream is enriched with $e^{\pm}$ pairs) is (e.g., Zhang, 2018)

$$\bar{\gamma} = \frac{\epsilon_e}{\xi_e}(\Gamma - 1)\frac{m_p}{m_e}\frac{n_p}{n_e}, \tag{5.21}$$

and γ_M is the maximum electron Lorentz factor, it is derived by balancing the rate of acceleration with the rate of radiative cooling at the shock, and it defined as (e.g.,

Zhang, 2018)

$$\gamma_M = \left[\frac{6\pi e}{\sigma_T B' \kappa (1+Y)}\right]^{1/2}, \tag{5.22}$$

where $\kappa \geq 1$ is a parameter that describes the efficiency of acceleration (Zhang, 2018). Electrons cool on a comoving cooling time:

$$t'_{\rm cool}(\gamma) = \frac{6\pi m_e c}{\gamma \sigma_T B'^2 (1+Y)}. \tag{5.23}$$

The electrons that cool over the dynamical time

$$t'_{\rm cool} = t'_{\rm dyn} \approx \frac{R}{\Gamma \beta c} \approx \frac{c\hat{t}}{\Gamma c} = \frac{\hat{t}}{\Gamma}, \tag{5.24}$$

have Lorentz factor

$$\gamma_c = \frac{6\pi m_e c}{\sigma_T B'^2 (1+Y)} \left(\frac{\Gamma}{\hat{t}}\right). \tag{5.25}$$

Rewriting equation 5.25 with the observer time $t_z \approx \hat{t}/\Gamma^2$

$$\gamma_c = \frac{6\pi m_e c}{\sigma_T \Gamma t_z B'^2 (1+Y)}. \tag{5.26}$$

The comoving magnetic field, B', is calculated by assuming that a fraction ϵ_B of the internal energy density of the shocked material goes towards the magnetic field energy density, and then it can be written as:

$$\frac{B'^2}{8\pi} = \epsilon_B (\Gamma - 1) n_2 m_p c^2 \approx \epsilon_B (\Gamma - 1)(4\Gamma n_1) m_p c^2 \approx \epsilon_B 4\Gamma^2 n_1 m_p c^2, \tag{5.27}$$

$$B' = \Gamma c \sqrt{32\pi m_p \epsilon_B n}, \tag{5.28}$$

where $n_2 = 4\Gamma n_1 = 4\Gamma n$, and $n = n_1$ is the upstream medium density. Now substituting equation 5.28 into equation 5.22 one finds the maximum electron Lorentz

factor:

$$\gamma_M = \left[\frac{6\pi e}{\sigma_T(\Gamma c\sqrt{32\pi m_p \epsilon_B n})\kappa(1+Y)}\right]^{1/2},$$
$$\gamma_M = \left(\frac{\pi}{2\epsilon_B n m_p}\right)^{1/4}\left(\frac{3e}{2\kappa\Gamma\sigma_T c(1+Y)}\right)^{1/2}. \tag{5.29}$$

Once one has these explicit relationships of the different Lorentz factors that characterize the regime of each part of the afterglow emission, one can use the equation 5.18 and find the characteristic break frequencies ν_m, ν_c and ν_a. One also has to realize that (as seen in the previous chapter) by having the functional form of synchrotron radiation one can automatically obtain the SSC part in the Thomson regime.

6 Numerical Simulations

In this chapter, I will present the numerical code developed by Gill and Thompson (2014) that helps calculate the afterglow emission. The integration with the equal arrival time surface is presented to calculate the observed flux density. Furthermore, the results of the numerical simulations of the afterglow emission of GRB 190114C are presented. Several emission processes are taken into account in the numerical code, and in this chapter I intend to compare different simulations that include different physical processes that generate the emission in the afterglow.

6.1 Numerical Method

In this work a numerical code is used, specifically a kinetic code that simulates the afterglow emission of gamma-ray bursts for an external forward shock developed by Gill and Thompson (2014). This numerical code has been used to study prompt emission in several published works, e.g., Gill and Thompson (2014); Gill and Granot (2018b); Vianello et al. (2018); Gill et al. (2020). The numerical code basically calculates the time evolution of the distributions of electrons and photons in an astrophysical plasma in the emission region (comoving frame). To do this, we must solve the relativistic kinetic equations for each type of particle species. These equations can be composed of differential and integral terms depending on the radiative process that is taken into account and, the equations found in the Sections 5.3-5.4. The rate of change of the photon spectrum and particle distribution due to different radiative process can be expressed as (e.g. Blumenthal and Gould, 1970; Pennanen et al., 2014; Fukushima

et al., 2017; Petropoulou and Mastichiadis, 2009; Belmont, 2009)

$$\frac{\partial N'_{\pm}}{\partial t'} = \dot{N}'_{\pm,\mathrm{coul}} + \dot{N}'_{\pm,cs} + \dot{N}'_{\pm,pp} + \dot{N}'_{\pm,pa} + \dot{N}'_{\pm,\mathrm{exp}} + \dot{N}'_{\pm,\mathrm{syn}}, \tag{6.1}$$

$$\frac{\partial N'_{\gamma}}{\partial t'} = \dot{N}'_{\gamma,cs} + \dot{N}'_{\gamma,pp} + \dot{N}'_{\gamma,pa} + \dot{N}'_{\gamma,\mathrm{exp}} + \dot{N}'_{\gamma,\mathrm{syn}} + \dot{N}'_{\gamma,\mathrm{esc}}, \tag{6.2}$$

where $N'_{\gamma}(x)$ is the photons number density distribution in the shocked region per unit dimensionless energy $x = \hbar\omega/m_e c^2$, and $N'_{\pm}(p)$ is the particles number density distribution in the shocked region per unit dimensionless momentum p (in units of $m_e c$). $\dot{N}'_{\mathrm{coul}}$ correspond to the Coulomb scattering density distribution rate, $\dot{N}'_{cs}$ is the Compton scattering density distribution rate, $\dot{N}'_{pp}$ is the pair production density distribution rate, $\dot{N}_{\mathrm{exp}}$ is a term that takes into account adiabatic cooling and density dilution, $\dot{N}'_{\mathrm{syn}}$ is the synchrotron density distribution rate that also includes synchrotron self-absorption, $\dot{N}'_{\mathrm{esc}} = N'/t_{\mathrm{esc}}$ is a term that accounts for the escape of photons from the emission region expansion, where $t_{\mathrm{esc}} = R/(\Gamma c)$, and $\dot{N}'_{pa}$ is the pair annihilation density distribution rate (for details, Blumenthal and Gould, 1970; Vurm and Poutanen, 2009; Gill and Thompson, 2014). Details of the terms of the different radiative processes are shown in appendix A.

It should be noted that at each time step, the code recalculates the value for the bulk Lorentz factor Γ and for the radius r. We divide the evolution of photon-pair plasma into two regimes, the small energy exchange and the large energy exchange. In the regime of small energy exchange, the so-called Fokker-Planck (F-P) equations are used, which for isotropic and homogeneous distributions can be written as (e.g. Nayakshin and Melia, 1998)

$$\frac{\partial {N'_{\pm}}^{F-P}}{\partial t'} = \frac{\partial}{\partial p}\left[\frac{\gamma_e}{p} A_{\pm} N'_{\pm}\right] + \frac{1}{2}\frac{\partial}{\partial p}\left[\frac{\gamma_e}{p}\frac{\partial}{\partial p}\left(\frac{\gamma_e}{p} D_{\pm} N'_{\pm}\right)\right], \tag{6.3}$$

$$\frac{\partial {N'_{\gamma}}^{F-P}}{\partial t'} = \frac{\partial}{\partial x}(A_{\gamma} N'_{\gamma}) + \frac{1}{2}\frac{\partial^2}{\partial x^2}(D_{\gamma} N'_{\gamma}), \tag{6.4}$$

where the advection coefficient A is the average rate of change of particle momenta and photon energy, and the diffusion coefficient D is the diffusivity of particle and photons in momentum and energy space. Both coefficients have contributions from Coulomb,

synchrotron self-absorption (SSA), and Compton scattering, and the advection terms from expansion:

$$[A, D]_{\pm} = [A, D]_{\pm,cs} + [A, D]_{\pm,\mathrm{coul}} + [A, D]_{\pm,\mathrm{SSA}} + A_{\pm,\mathrm{exp}}, \tag{6.5}$$

$$[A, D]_{\gamma} = [A, D]_{\gamma,cs} + [A, D]_{\gamma,\mathrm{SSA}} + A_{\gamma,\mathrm{exp}}. \tag{6.6}$$

The use of the F-P approximation is essential to deal with Coulomb collisions between thermal pairs, and the Compton scattering when the energy exchange between the electron and photon is small (see for details Gill and Thompson, 2014). For the resolution of equations 6.3 and 6.4, the fully implicit finite difference scheme of Chang and Cooper (1970) was chosen. This scheme was chosen for its robustness and guarantee of producing positive spectra. Although its precision is of the first order, its stability is more reliable even than higher order schemes. For the distribution of particles, logarithmic grids were used that cover eleven orders of magnitude ($p = 10^{-3} - 10^{8}$) in momentum and fifteen orders ($x = 10^{-8} - 10^{7}$) in energy, with a grid size of 320 points for both distributions. The boundary conditions that are imposed are those of vanishing particle and photon flux, since the number of particles and photons is conserved. With the Chang-Cooper scheme (e.g., Chang and Cooper, 1970), one has the advantage that one doesn't have to use the Courant condition, which depends on the size of the smallest energy/momentum bin for logarithmic grids. The timestep must be smaller than the smallest cooling timescale in the problem, i.e., synchrotron/Compton cooling, to ensure an accurate time-evolution of the particle distribution. The computational time of the simulations depends on the amount of observation data available, in the case of GRB 190114C there are data of up to 2454 seconds (see Section 6.4) this means that the simulation needs a computational time of two hours.

6.2 The observed radiation

To calculate the spectral flux density $F_\nu(\nu, t)$, where t is the observer time, we first need to know the relation of the shell's isotropic equivalent comoving spectral luminosity $L'_{\nu',\rm iso}$ with the comoving synchrotron emissivity $j'_{\nu',\rm iso}$ (power per unit frequency per unit volume), because, the emissivity ($j'_{\nu',\rm iso}$) can be obtained from the numerical code presented in the previous section. This relationship is given through the volume of the emitting region

$$\frac{L'_{\nu',\rm iso}}{j'_{\nu',\rm iso}} = V' = 4\pi R^2 \Delta' = \frac{\pi R^3}{(3-k)\Gamma}. \tag{6.7}$$

Furthermore, the effect of the equal-arrival-time surface (EATS, see Figure 6.1) must be taken into account (e.g., Zhang, 2018). The equal arrival time surface is a physical surface where photons emitted at different angles to the line-of-sight, with different radii, and at different lab-frame times, arrive at the distant observer at the same time (see Figure 6.1). This is an important effect that is due to the geometry of the problem, which is not taken into account in many works (e.g., Derishev and Piran, 2021, 2019; Veres et al., 2019; Joshi and Razzaque, 2021; Joshi et al., 2023). The arrival time t to a distant observer of a photon emitted at radius R and angle $\bar{\theta} = \cos^{-1}(\hat{R} \cdot \hat{n})$ from the line-of-sight (LOS), where $\hat{n}$ is the unit vector pointing towards direction of the observer, from a source located at redshift z corresponding to a luminosity distance $D_L(z)$ is given by

$$t = \frac{t_z}{(1+z)} = \hat{t} - \frac{R\bar{\mu}}{c}, \tag{6.8}$$

where $\bar{\mu} = \cos\bar{\theta} = \hat{R} \cdot \hat{n}$. For the thin-shell approximation, it is taken that the thin-shell is located at a normalized radial distance $\chi = R/R_{\rm dec}$ from the central source at the lab-frame time (e.g., Gill and Granot, 2018a)

$$\hat{t} = \frac{R_{\rm dec}}{c} \int_0^\chi \frac{d\chi'}{\beta(\chi')}, \tag{6.9}$$

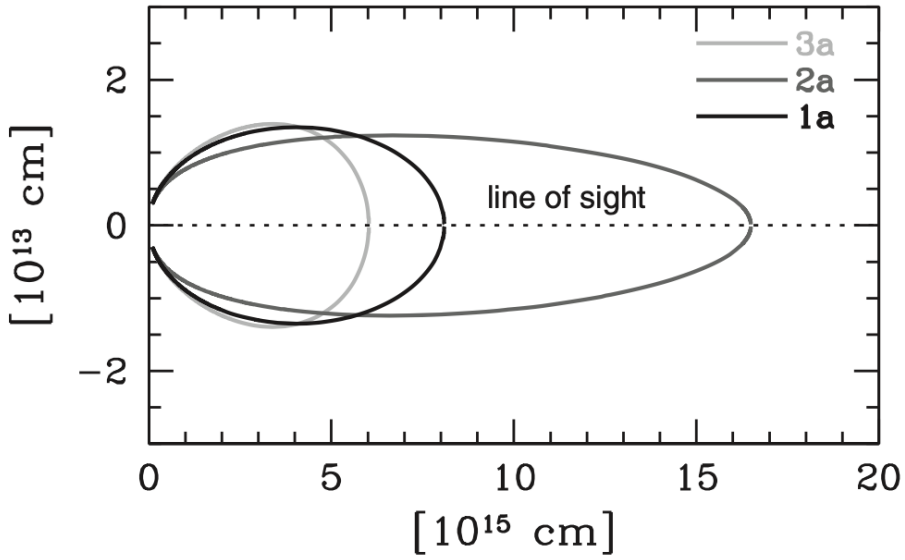

Figure 6.1: A 2D cross-section of a 3D equal-arrival-time surface (EATS) for a relativistic spherical shell (e.g., Zhang, 2018). Photons emitted along the EATS at different angles away from the line-of-sight, and correspondingly from different radii and at different lab-frame times, arrive at the distant observer at the same time.

where $\beta = \sqrt{1 - \Gamma^{-2}}$.

Finally, the spectral flux can be expressed using the isotropic comoving spectral luminosity $L'_{\nu'}$ as (e.g., Gill and Granot, 2018a; Zhang, 2018)

$$F_\nu(\nu, t) = \frac{(1+z)}{16\pi^2 D_L^2} \int \bar{\delta}_D^3 L'_{\nu',\mathrm{iso}} d\bar{\Omega}, \tag{6.10}$$

where $d\bar{\Omega} = d\bar{\mu} d\bar{\varphi}$ is the differential solid-angle subtended by emitting region relative to the central source, and

$$\bar{\delta}_D = \frac{1}{\Gamma(1 - \vec{\beta} \cdot \hat{n})} = \frac{1}{\Gamma(1 - \beta\bar{\mu})}, \tag{6.11}$$

is the Doppler factor, where in the second expression it is assumed that the flow expands radially, so that $\hat{\beta} = \hat{R}$. The relation of $\nu_z = \nu(1+z)$ and ν' is $\nu_z = \bar{\delta}_D \nu'$.

PARAMETERS FOR ANALYTIC AND NUMERICAL MODELS						
$E_{\rm iso}$ [erg] $\times 10^{53}$	Γ_0	n [cm^{-3}]	p	ϵ_e	ϵ_B $\times 10^{-5}$	ξ_e
8.0	500	0.77	2.2	0.1	370	1

Table 6.1: Parameters

6.3 Analytic vs. Numerical

The first step was to implement an analytical model which helps to know how sensitive are the different parameters that are used to configure the spectrum of a GRB ($E_{\rm iso}$, Γ_0, n, p, ϵ_e, ϵ_B, ξ_e), knowing this helped me to calibrate the numerical code. I used the analytical model of Sari and Esin (2001), which is a piece-wise power law model for the flux. This model only takes into account synchrotron emission and synchrotron self-Compton emission. It is characterized by the frequencies discussed in the previous chapter, that is, ν_m, ν_c, and ν_a (eqs. (4.26)-(4.30)) for the synchrotron part and ν_m^{IC}, ν_c^{IC}, and ν_a^{IC} for the synchrotron self-Compton part (eqs. 4.43-4.45). It takes in a set of model parameters to produce the afterglow emission, namely $E_{\rm iso}$, Γ_0, n, p, ϵ_e, ϵ_B, and ξ_e. I used a fiducial set of parameters, as shown in Table 6.1, to compare the analytical and numerical models. What I compare of both models are the spectra that they generate with the same parameters and at the same time. For the numerical simulation, all the physical processes that are not included in the analytical model of (Sari and Esin, 2001) were disabled, i.e., the physical processes used in the numerical simulations are the synchrotron and the synchrotron self-Compton.

Figure 6.2 shows the comparison between the spectrum generated by the numerical and analytical model. The black curve is the spectrum of the numerical model and the blue light lines are the spectrum of the analytical model. Both models are set to 90 seconds, and the set of parameters used to generate these spectra in both models is the same, that is, both use the parameters in Table 6.1. The reason why I chose 90 seconds to fix both spectra (numerical and analytical) is because the computation

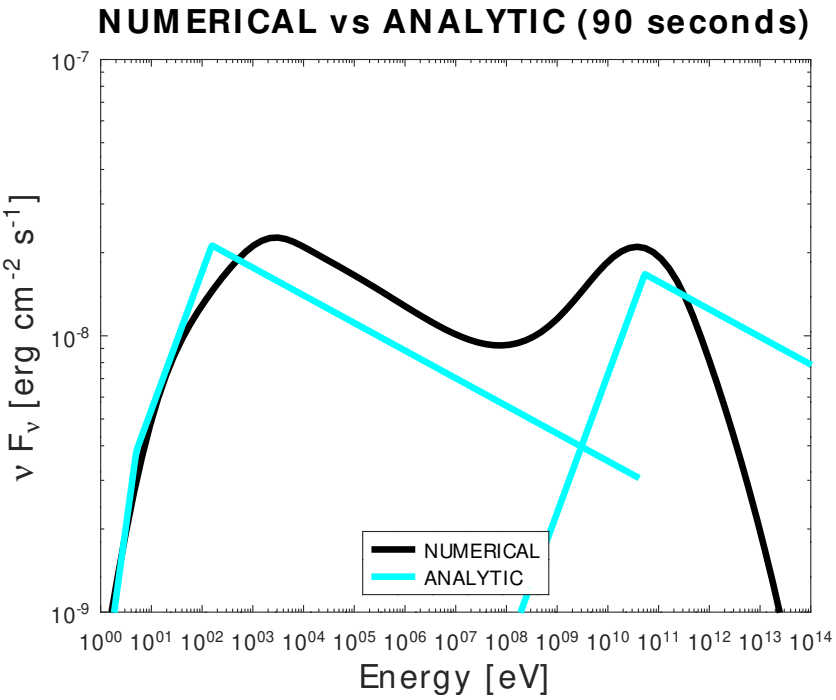

Figure 6.2: Comparison of spectra obtained with numerical and analytical models. The parameters are shown in Table 6.1.

time is shorter, since to do the numerical simulation it only takes about 15 minutes. One can notice the fits are somewhat different because the analytic and the numerical model have different assumptions. To start setting parameters for a GRB, the analytic model is useful to get the approximate values of the parameters, while the numerical model is better because it takes into account more processes. One important thing to note though is that the synchrotron and SSC peaks differ in both models. The shape of the slopes of the synchrotron part (left in Figure 6.2) is the same as in the numerical simulation, only that the peak has a lower energy. The SSC peaks (right in Figure 6.2) from the analytical and numerical model have the same energies but differ in flux. This is because in the analytical model to calculate the SSC part many simplifying approximations are made (for example, see Section 4.2) while in the numerical code the exact equations are taken. But, the main difference is probably due to the fact that in the analytical model the total number of electrons is conserved, while in the numerical model fresh electrons are continuously injected at the shock front.

6.4 GRB 190114C

The main purpose of this thesis work is to give a methodology, using exact equations in the numerical code (see Section 6.1) and the implementation of the equal arrival time surface (see Section 6.2), that is then used to explain the afterglow of GRBs that show a very high energy component. Here we investigate the afterglow of GRB 190114C that has a redshift of $z = 0.4245$ which corresponds to a luminosity distance of 2.3 Gpc. It was the first GRB for which detection of tera-electronvolt (TeV) photons was reported in the literature by the MAGIC telescope in the $0.2 - 1$ TeV energy range between 62 s and 2454 s after trigger (e.g., Veres et al., 2019). The detection of TeV bright GRBs is important, because it provides further insight into the shock microphysics at relativistic collisionless shocks as well as the global energy budget of the burst. Since the softer emission is purely synchrotron, the interpretation of the VHE emission being synchrotron self-Compton (SSC) follows naturally (e.g., Fraija et al., 2019a,c; Sari and Esin, 2001; Asano et al., 2020; Joshi and Razzaque, 2021; Derishev and Piran, 2019).

The afterglow of this GRB has been modeled in a number of works, e.g., Joshi et al. (2023) could explain VHE gamma-ray observations using the synchrotron and SSC models and that a refreshed shock is required. They also concluded that the absorption of VHE photons for pair production in the blast wave is negligible. Derishev and Piran (2021) include exact KN corrections, pair production via self-absorption of the high-energy photons, and the corresponding emission of these pairs. Asano et al. (2020) found that the circumburst medium is likely an ISM, rather than a stratified stellar wind, and that the IC component of the afterglow emission is as strong as the synchrotron emission. They also found that detection at late times also implies that KN suppression and $\gamma\gamma$ absorption to VHE emission does not increase with time. Being able to detect the SSC component in these types of GRBs is important for the study of the shock energy distributions in electrons and magnetic fields, and the environment surrounding the GRBs (e.g., Joshi and Razzaque, 2021).

The parameters of the model are obtained at the earliest time interval (see Table

6.2). In the panels of Figure 6.3 the black curve is the spectrum with the theoretically highest value of γ_M (equation 5.29), i. e., with $\kappa = 1.0$, the blue-light curve is the same spectrum with $\kappa = 10.0$, and the red curve is the same with $\kappa = 20.0$. It can be noticed that the value of the energy flux located between the two peak fluxes is lower when κ is higher. This is because when κ is higher, γ_M is lower, and therefore the exponential decay of the flux for $\nu > \nu_M$ occurs at smaller frequencies compared to when $\kappa = 1.0$. As suggested by panels (a) and (b), the ideal κ value for this spectrum would have to be between the values $1.0 < \kappa < 10.0$, since in this range the model spectrum passes through the 1-σ error regions at around 0.1 GeV . Panel (a) needs a higher κ value, while panel (b) needs a value closer to the theoretically lowest value of κ (i.e. $\kappa = 1.0$), so a value between $1.0 < \kappa < 10.0$ would be the best choice. Values higher than $\kappa = 20.0$ can be discarded because, as observed in panel (b) (red curve), for this value of κ the spectrum moves away from the central observational data. The model is evolved to the later time intervals available in the observational data. When comparing the model with the observations of GRB 190114C, it is not intended to derive the best-fit model parameters using advanced fitting methods, but only to obtain a reasonably good match between the model and observational data for sensible model parameters, although in Section 6.5 an analysis is performed to compare how good the fit is at 75 seconds.

As one can see in Figure 6.3, the afterglow spectrum produced by the numerical model matches the data well at all times. In particular, if one looks at panels (a) and (b) of the Figure 6.3, one can notice that the numerical model matches the SSC part with the observational data well. The observations at intermediate energies are those that show the worst match with the numerical simulation. The fact that the temporal evolution of the afterglow emission is well match by the numerical model, shows that the afterglow is produced mainly by synchrotron and SSC radiation, with injection of electrons at the shock front, as assumed in the model (e.g. Derishev and Piran, 2019; Fraija et al., 2019a; Wang et al., 2019; Zhang et al., 2020). Another thing is that one can see in Figure 6.3, that the peak flux of synchrotron emission at longer times is smaller than the peak flux of the SSC part (e.g., see panel (e)), this is due to the fact

that the Compton-Y parameter changes with time.

In Figure 6.4 one can see the afterglow spectrum divided into its two different components, the blue dashed line is the synchrotron emission part, the red dashed line is the SSC emission part, and the black line is the total spectrum. This spectrum is at 75 seconds where we have observations from both components (see Figure 6.3). Dividing the spectrum into its two parts one can notice that the synchrotron component is dominant in the energy range of 0.01 keV to 10 GeV, while the SSC part is dominant in the energy range of 1 GeV to 10 TeV. This is consistent with the observational data and with what has been shown by works such as, Sahu and Fortín (2020); Wang et al. (2019); Asano and Mészáros (2012); Veres et al. (2019).

To test the importance of the other radiative processes. I first performed simulations without the scattering due to Coulomb effects and in this case the result did not change, this implies that the Coulomb effects are not important at least for GRB 190114C. Then I proceeded to do a simulation without the production and annihilation of pairs, the results of this simulation are shown in Figure 6.5. In this figure, I show the afterglow spectrum at time 75 seconds (panel a) and at time of 140 seconds (panel b). Without pair production, the SSC part at 75 and 140 seconds moves a bit to higher energies, this shows that for the afterglow emission of GRB 190114C, pair production is not a physical process that significantly influences the results. Although the pair production is not significantly important, there are differences in the spectra that are shown in the Figure 6.5. Therefore, this process must be taken into account if higher precision is desired in numerical simulations. In particular, doing these simulations without pair production and Coulomb scattering makes it clear that depending on which high-energy physical processes are added to the model, the physical processes that are really important in fixing the set of parameters (Table 6.2) are synchrotron and SSC. These simulations demonstrate that the afterglow emission from GRB 190114C cannot be explained with the synchrotron component alone and the SSC process is required to explain the very high energy component in the afterglow emission, but note that it is required the condition $\epsilon_B \ll \epsilon_e$ ($4 \times 10^{-3} \ll 0.21$, my parameters in Table 6.2) to raise the value of the Compton-Y parameter high

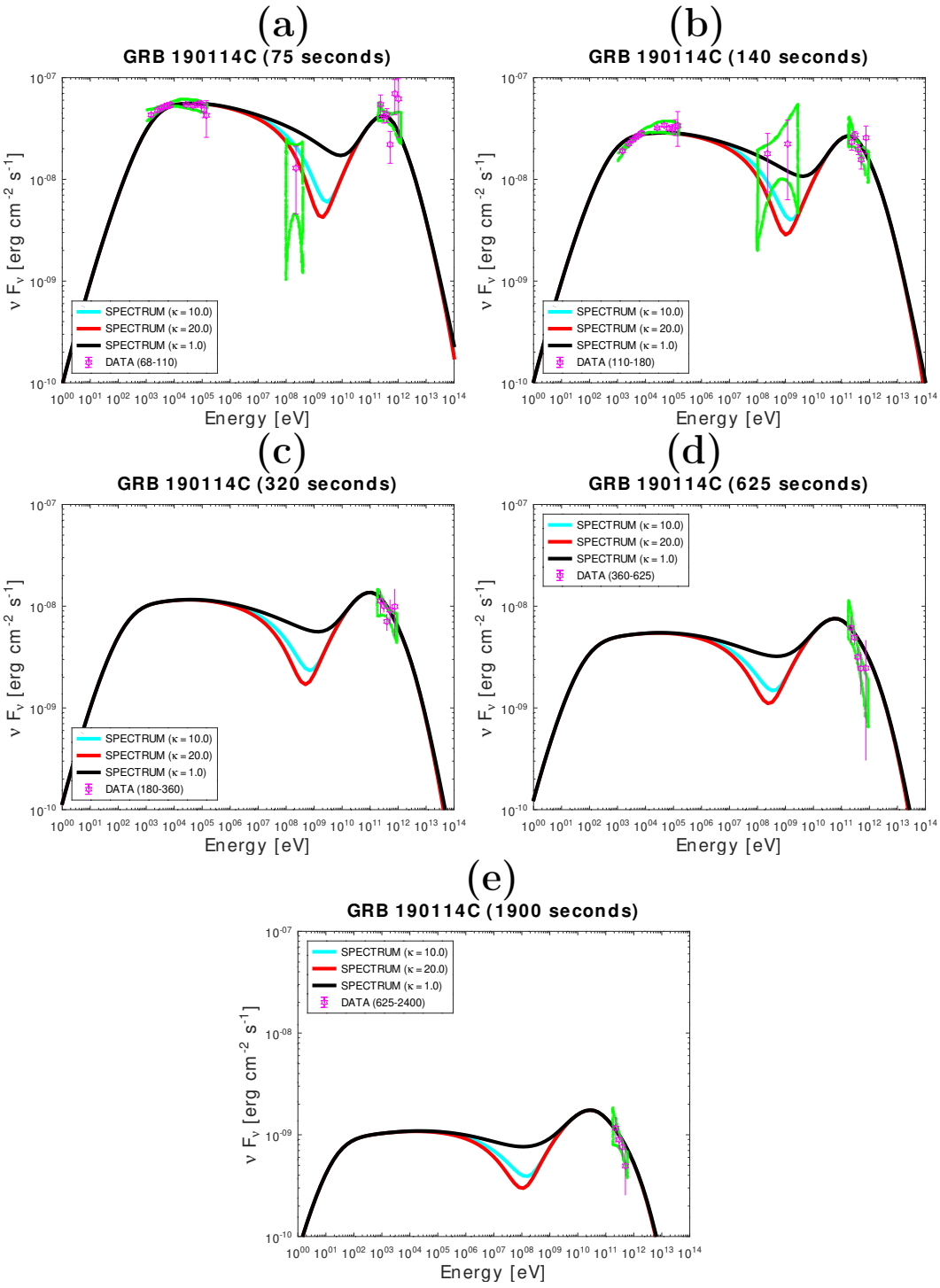

Figure 6.3: GRB 190114C spectrum for different times (after correction for extinction due to the extragalactic background light). The black lines are the simulations and the green regions are the 1σ error regions of the data in different energy bands collected by different detectors of MAGIC (2019). The red curves are the case with $\kappa = 20.0$ and the blue-light curves are the case with $\kappa = 10.0$.

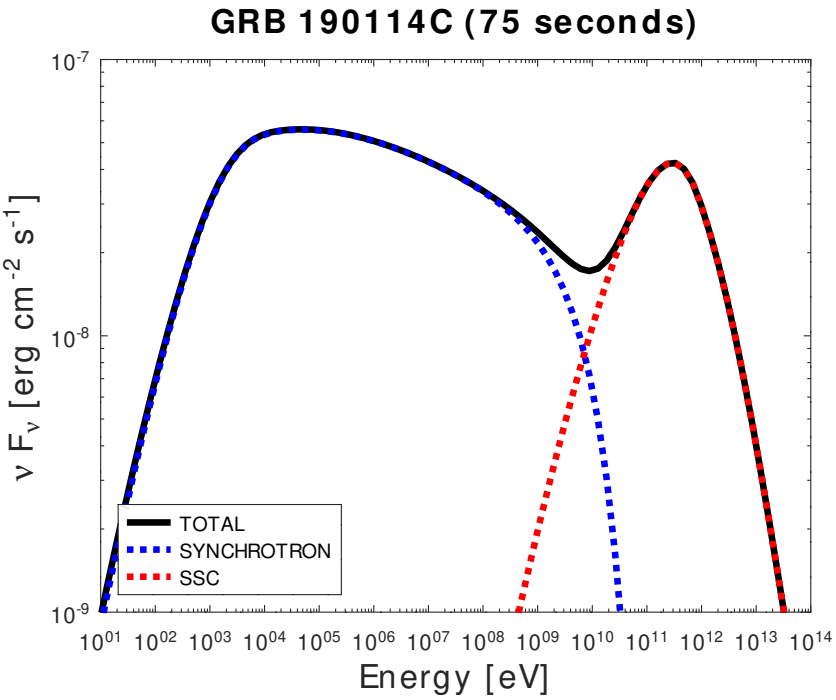

Figure 6.4: GRB 190114C spectrum at 75 seconds. Only the synchrotron part (blue dashed line). Only synchrotron self-Compton part (red dashed line), and total spectrum (black line).

enough above unity to make the SSC component detectable (e.g., Wang et al., 2001; Zhang and Mészáros, 2001; Zhang et al., 2021; Sari et al., 1998).

In Figure 6.6 I show the observed light curve of GRB 190114C integrated over the energy range 0.3-1 TeV (green points). The black curve is the light curve generated by the integrated numerical code over 0.3-1 TeV in a time range of 68 to 2400 seconds. There seems to be a break at approximately 900 seconds, where the slope of the light curve is steeper. This break does not have a clear origin. It cannot be the standard achromatic jet break, which is a geometric effect and affects all wavelengths, since we do not see a similar break in the X-ray data. Therefore, its origin must be either spectral or numerical and needs to be investigated further. In the energy range 0.3 to 1 TeV (MAGIC observations), the light curve produced by the numerical simulation (black line) matches the data well.

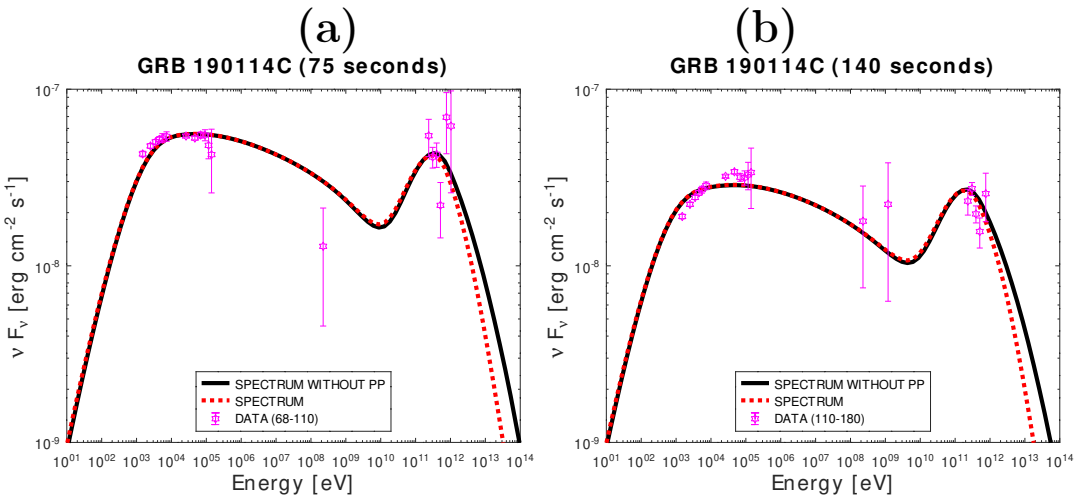

Figure 6.5: The black curves are GRB 190114C spectrum at 75 seconds (a) and 140 seconds (b), but with pair production and pair annihilation processes disabled in the numerical simulation. The red dashed curves are the original spectra of figure 6.3.

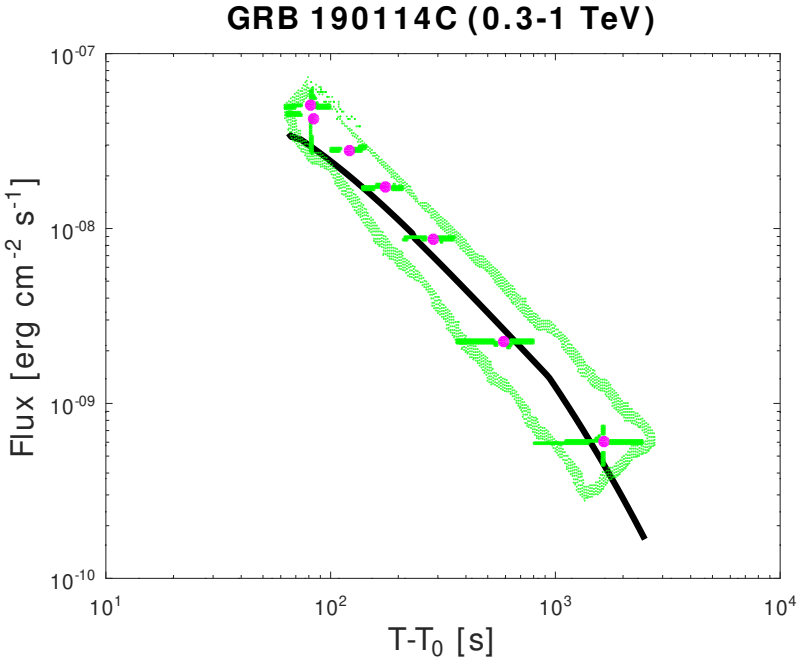

Figure 6.6: Light curve of GRB 190114C. Green points enclose the 1σ error region of the MAGIC data (0.3-1 TeV) and the black line is the lightcurve from the numerical simulation for $E = 0.3 - 1\,\mathrm{TeV}$.

6.5 Comparison with Other Works

Table 6.2 contains a compilation of the microscopic parameters that were used in various works for the GRB 190114C. For comparison, I took the spectrum data from different authors' models and plotted them together with my results (see Figure 6.8). The last column of Table 6.2 indicates the color of each curve in Figure 6.8.

To quantify how well the spectra shown in Figure 6.8 agree with the observational data, a simple analysis is made taking into account only the energy flux in the range of 68-110 seconds since It is in this range that there are more spectra from different authors (e.g. Joshi and Razzaque, 2021; Asano et al., 2020; Derishev and Piran, 2021; Veres et al., 2019). The main objective of this analysis is to see how close the spectra of the different authors are to the observational data with their respective error. For this I use a simple distance formula between two points and make it dimensionless by dividing it by the model, that is, I calculate the relative error (e.g., Abramowitz and Stegun, 1964; Weisstein, Eric W., 2023):

$$\epsilon_{\text{relative}} = \frac{\text{Observed} - \text{Model}}{\text{Model}} \pm \frac{\text{Error}}{\text{Model}} \tag{6.12}$$

where the observed points are the calculated energy flux at the center of the energy bin (erg cm^{-2} s^{-1}) with their respective error ("Error" in equation (6.12)) and, the model points are the spectra of each author shown in the figure 6.8. Figure 6.7 shows graphs of relative error (eq. (6.12)) vs. energy (eV), these plots show more clearly how close the spectra are to the observation data. There are 19 points because, as can be seen in the Figure 6.7, the observational data are 19 (magenta points). The worst case is clearly that of Joshi and Razzaque (2021) that corresponds to panel (c) of the Figure 6.7, in fact there are two points that are not shown that exceed 100 units on the "$\epsilon_{relative}$" axis. These points correspond to the SSC part, as can be seen in Figure 6.8c, where it is also the part that matches the observational data the worst. In the case of Derishev and Piran (2021) one can observe in panel (d) of the Figure 6.7 two points ($\sim 10^{12}$ eV) that are further away from the observational

data compared to panels (a), (b) and, (e). The error bar of one of these points even reaches 5 units on the "$\epsilon_{relative}$" axis while in the cases (a), (b) and, (c) the 3 units are not exceeded, these points correspond to the SSC part of the Figure 6.8d. The cases (a), (b) and, (e) of Figure 6.7 are really similar, although noting that in panel (a) that corresponds to the case of Asano et al. (2020), the observation data of the synchrotron part (i.e. approximately in the range of 1×10^3 to 1×10^{-5} eV on the "energy" axis) deviate more from the observational data than the others panels. This is reflected in the Figure 6.8a in the synchrotron part. The only significant difference between panels (a), (b) and (e) is the observed point at -1 on the "$\epsilon_{relative}$" axis in panels (a) and (b). Panel (e) which is the case of this thesis does not show this point that corresponds in the Figure 6.8 to the synchrotron part of the spectra of Asano et al. (2020) and Veres et al. (2019).

Now paying attention to the Figure 6.8, in panel (a) it can be seen that the synchrotron emission component is lower and thinner than my numerical model, while the SSC component has a similar peak flux, but this component reaches higher energies, but as shown in the analysis above, the SSC components match up quite well. The assumptions that Asano et al. (2020) have are the same as in this thesis, the main difference may be due to their numerical implementation of the inverse Compton scattering process, as this can be problematic in certain regimes (e.g., Belmont, 2009) and require more careful treatment, as is done in the code used for this thesis work. In panel (b), it can be seen that it is the case that most resembles my numerical model, as can be seen in panels (b) and (e) of Figure 6.7, in particular, SSC components match well. The synchrotron emission component is also a good match, although the blue curve is a bit less wide. The Veres et al. (2019) model assumes synchrotron and SSC losses, adiabatic losses, $\gamma\gamma$ absorption, emission from pairs, and synchrotron self-absorption. The main difference with my numerical model is that they do not integrate over the equal-arrival-time surface. In panel (c) it can be seen that this model has the worst match with my numerical model, as well as being the worst match to the observational data as seen above. The synchrotron component is discrete and the peak flux in the SSC component is quite smaller than shown in

other models. This is because the model presented by Joshi and Razzaque (2021) is an analytical model, but this analytical model, in addition to taking into account the synchrotron and self-Compton processes, uses the Blandford & Mckee dynamics, and to model the KN suppression it uses a cut-off SSC photon energy in the Thomson regime, and takes into account the internal absorption in the blastwave. In panel (d), it can be seen that the match between the two models is not too bad, although the biggest differences are that the synchrotron component is thinner in the red curve and the SSC component peak has higher energy flux but lower energy compared to my spectrum (see Figure 6.8d). In fact, the peak in the SSC part of the spectrum presented by Derishev and Piran (2019) is larger than all other models, as can be seen in Figure 6.7, the points of the SSC component for the Derishev and Piran (2019) model are worse than those of Asano et al. (2020), Veres et al. (2019), and this thesis. In particular, the main difference with my numerical model would be that in Derishev and Piran (2019) use a steady state model and do not evolve the bulk Lorentz factor at all.

GRB 190114C has also been modeled with a stratified stellar wind medium (e.g., Fraija et al., 2019a,c; Yamasaki and Piran, 2022; Ravasio et al., 2019; Acciari et al., 2020; Asano et al., 2020) because this GRB is associated with a core collapse of a Wolf-Rayet star (LGRB). Weaver et al. (1977) studied the structure of the interaction of a stellar wind and the ISM, where they found a phase transition between the stratified stellar wind to ISM approximately at distances greater than 10^{-2} pc. It has been studied that the transition from stellar wind to ISM is present in GRBs (e.g., Fraija et al., 2019a,b; Li et al., 2020).

We have compared with the models of GRB 190114C by different authors. In particular the model that has the most assumptions in common with my numerical model is the Asano et al. (2020) model. In Figure 6.9 I show spectra for the Asano et al. (2020) parameters (Table 6.2). The light-blue curve is the curve that Asano et al. (2020) show in their work. The black curve is the spectrum generated by the numerical code used in this thesis, with the Asano et al. (2020) parameters. Comparing the spectra in Figure 6.9, it can be seen that both Asano et al. (2020)'s numerical model and

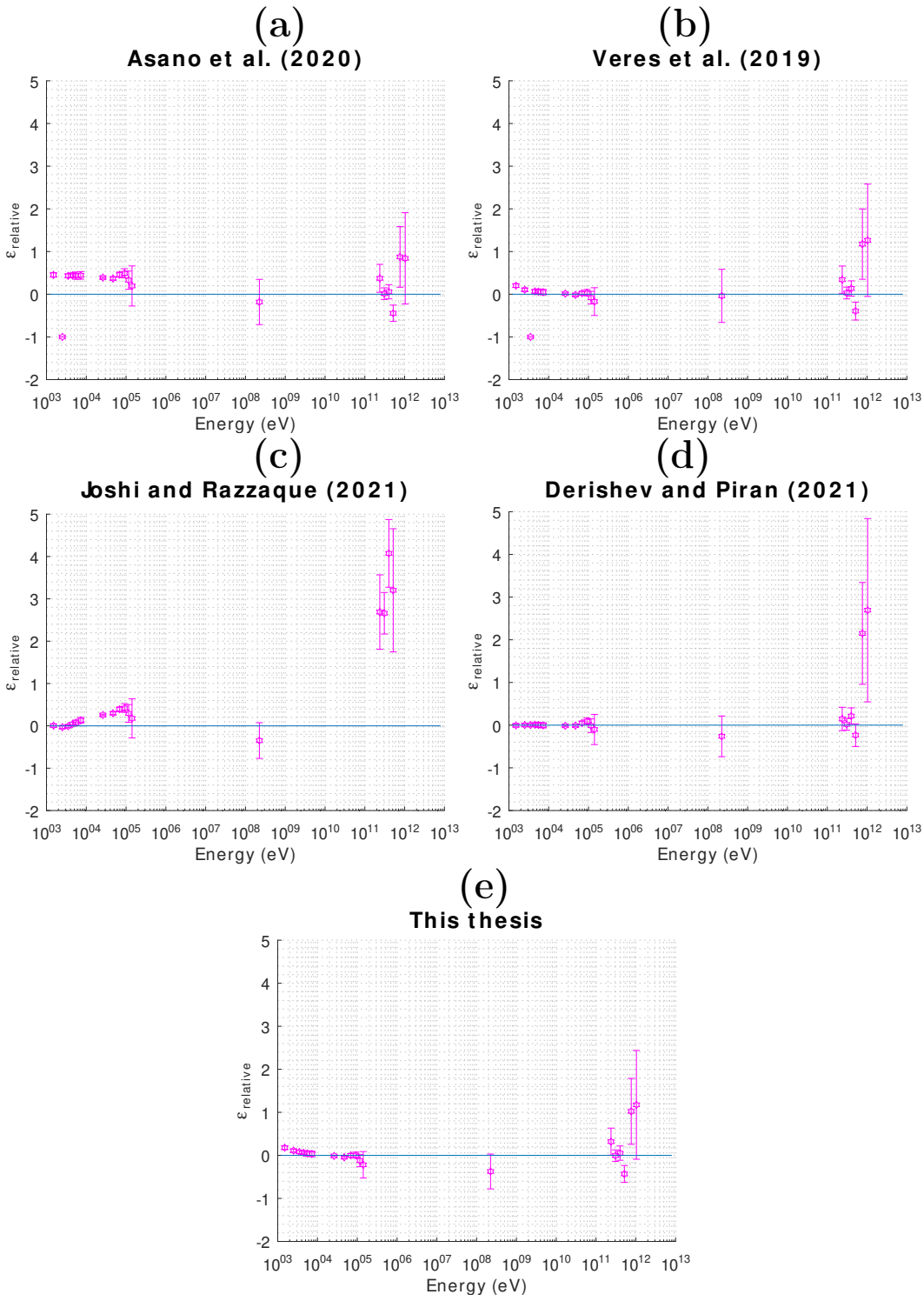

Figure 6.7: Relative errors vs. energy for the different models, for data in the range 68-110 seconds).

GRB 190114C								
E_{iso} [erg] $\times 10^{53}$	Γ_0	n [cm^{-3}]	p	ϵ_e	ϵ_B $\times 10^{-5}$	ξ_e	Ref.	Fig.6.8
4.2	400	1.5	2.2	0.21	400	1	This thesis	(black)
8	300-700	0.5	2.6	0.07	8	1	[Veres et al. (2019)]	(blue)
10.0	600	1.0	2.3	0.06	90	0.3	[Asano et al. (2020)]	(blue light)
40.0	300	0.02	2.18	0.033	1200	1	[Joshi and Razzaque (2021)]	(green)
3	109	2.0	2.5	0.13	620	1	[Derishev and Piran (2021)]	(red)

Table 6.2: Parameters

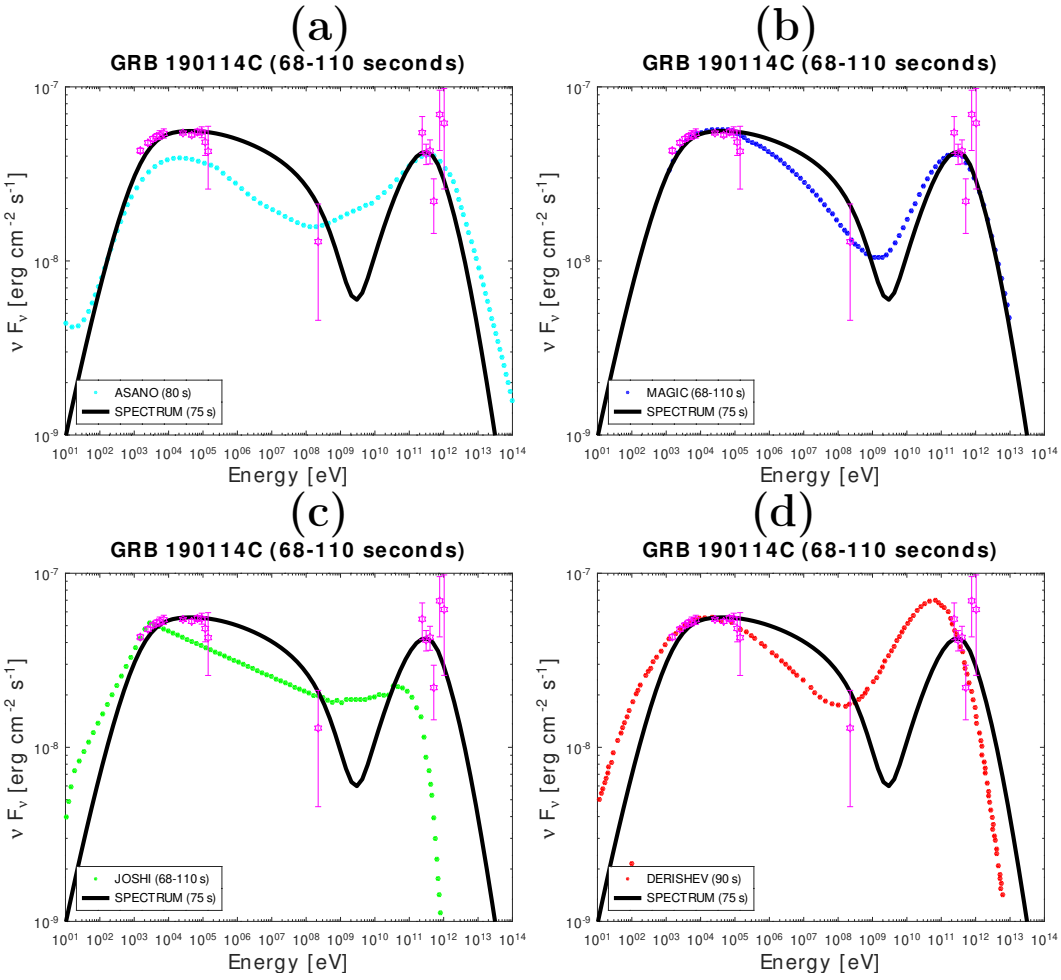

Figure 6.8: GRB 190114C model spectra from different works. The black curve shows the spectrum obtained from the numerical model in this thesis for parameters different from that in the works compared here (see Table 6.2). Panel (a) shows the spectrum from Asano et al. (2020) (blue light line). Panel (b) shows the spectrum from Veres et al. (2019) (blue line). Panel (c) shows the spectrum from Joshi and Razzaque (2021) (green line). Panel (d) shows the spectrum from Derishev and Piran (2021) (red line).

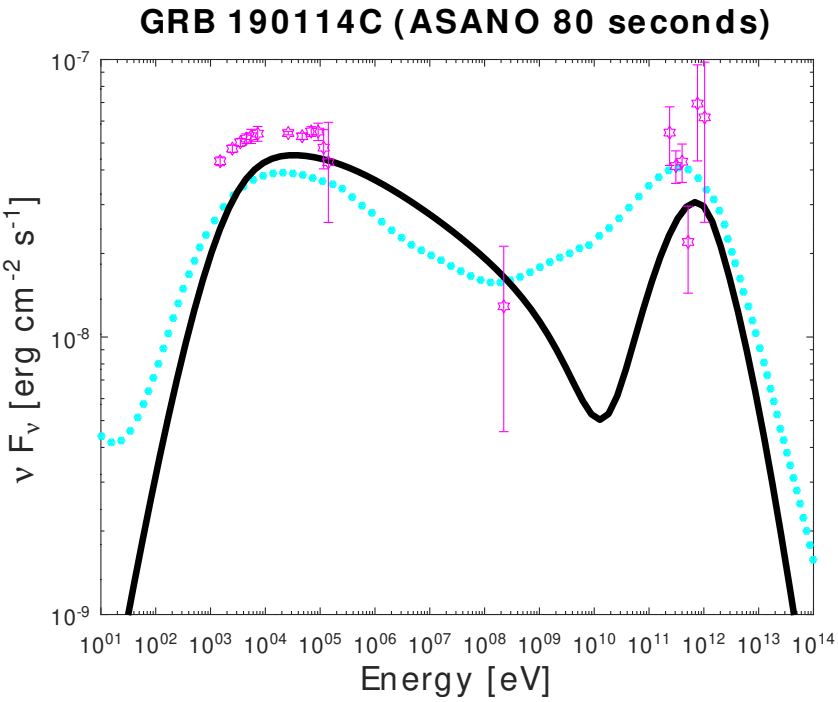

Figure 6.9: GRB 190114C spectrum. The light-blue curve is the spectrum from Asano et al. (2020) for an ISM external medium (method I in their paper). The black curve is the spectrum obtained by the numerical model used in this thesis for the same parameters as Asano et al. (2020).

mine can explain the GRB 190114C. As mentioned above, the main difference is how the Compton scattering cross section is implemented. In this thesis work an exact form is taken to calculate the cross section (see equations 27-39 of Belmont (2009)) while in Asano et al. (2020) an approximate form is taken (see equation 8 of Asano and Mészáros (2011)). The most sensitive parameter to adjust the peak of the SSC component is ϵ_B, it is important to note that in the Figure 6.9 the peak of the SSC component of the black curve is lower than that shown by Asano et al. (2020) in their results but, since the black curve takes exact equations to calculate the Compton scattering cross section, a larger value of ϵ_B is suggested than shown by Asano et al. (2020), i.e., $\epsilon_B > 9 \times 10^{-4}$.

7 Conclusions

In this thesis work, I have modeled the very high energy emission of GRB 190114C. First, I used a simple analytic model of synchrotron and synchrotron self-Compton emission to estimate the physical parameters of the relativistic jet and the surrounding medium. Then, I used a numerical code that produces more accurate and realistic GRB spectra in the jet's comoving frame by including important radiative processes, namely synchrotron and synchrotron self-Compton emission, electron injection at the shock front, pair production and annihilation, and Coulomb scattering. The results of this code were then post-processed where I integrated the comoving emission over the equal-arrival-time surface to compute the observed flux.
I found that:

- The afterglow emission from TeV-bright GRBs cannot be explained by the synchrotron component alone, at least in the leptonic model explored here. Its origin requires an additional spectral component, which is modeled here as synchrotron self-Compton. This component occurs quite naturally, but requires $\epsilon_B \ll \epsilon_e$ to raise the Compton-Y parameter enough above unity to be detectable.

- The set of model parameters that I found is consistent with the typical parameters found for a larger sample of GRBs. The ISM density is typical for long GRBs (which are found in star-forming regions), and to produce VHE emission from long GRBs, no special conditions are needed. The parameter that determines the radiative efficiency of the afterglow is ϵ_e and in various works it was found that its mean value is ~ 0.2 which is very close to 0.21 (my parameter) (e.g. , Sironi and Spitkovsky, 2010; Santana et al., 2014). The value of ϵ_B can

vary greatly in different GRBs in the range $10^{-8} \leq \epsilon_B \leq 10^{-3}$ with a mean value of $\epsilon_B \sim 10^{-5}$ (e.g., Santana et al., 2014)

- The set of parameters I found is not unique, that is, the parameter space of the model is degenerate. This is a common problem with afterglow model fitting, as the problem is always less constrained than the model parameters. To find the statistical uncertainty in the parameters of the derived model, many works use Markov Chain Monte Carlo (MCMC) methods that were not used here due to high computational cost and time investment (e.g., Cardone et al., 2010; Hajela et al., 2019).

- Table 6.2 shows the models from other works, evidencing the problem of parameter space degeneracy. The underlying issue is that different assumptions are made in numerical or analytical treatments. Therefore, it is necessary to use a single method to fit a sample of GRBs with VHE emission in order to obtain consistent solutions and reveal important trends that could lead to the production of VHE emissions.

- The numerical model employed in this thesis gives a reasonably good fit to the observed high energy emission of GRB 190114C at different times as shown in the Figure 6.3.

- By cancelling different processes in the numerical code, one can see that Coulomb scattering is negligible for this source. Instead, it is important to take into account the high energy photons spent in the process of pair production and annihilation to produce the observed level of IC peak.

7.1 Future Work

I plan to extend the work presented in this thesis to include the study of other GRBs and other physical processes of high energy emission including the following points:

1. Extend the current model to a general radial density profile ($\rho \propto R^{-k}$) for $0 \leq k \leq 2$ and investigate the stellar wind scenario ($k = 2$) in particular which is more relevant for long GRBs.

2. Make a detailed comparison with other published works that employ a similar numerical code to calculate the broadband spectrum.

3. Do a parameter space study for several GRBs with VHE emission to see which part of the parameter space is conducive to producing high energy emission in GRBs.

4. Make spectral and lightcurve fits to other GRBs that show VHE emission like GRB 180720B (e.g., Fraija et al., 2019b, 2021; Wang et al., 2019) and GRB 190829A (e.g., Salafia et al., 2022; Dichiara et al., 2022; Zhang et al., 2021).

5. Investigate the role of pre-accelerated pair loaded medium in front of the blast wave that can produce GeV and TeV emission, e.g., in Beloborodov (2005); Thompson and Madau (2000); Beloborodov (2000).

6. Investigation of hadronic models that can produce VHE emission in GRBs (e.g., Fraija, 2014; Sahu et al., 2022; Asano and Mészáros, 2012; Razzaque, 2010; Crumley and Kumar, 2012; Murase et al., 2012).

A Numeric Code Details

A.1 Adiabatic cooling and density dilution

In the equations 6.1 and 6.2, one has the terms $\dot{N}'_{\pm,\rm exp}$ and $\dot{N}'_{\gamma,\rm exp}$, which are the terms that take into account the adiabatic cooling of particles and photons due to the expansion of the emission region, also due to the expansion are the terms that account for the dilution density of the particles/photons. Adiabatic expansion is given by the equation (e.g., Gill and Thompson, 2014; Pennanen et al., 2014; Longair, 2010)

$$\frac{\partial N'(E',t')}{\partial t'} = \frac{\partial}{\partial E'}\left(-\frac{dE'}{dt'}N'(E',t')\right) - \frac{d\ln V'}{dt'}N'(E',t'), \tag{A.1}$$

where E' is a general energy and $d\ln V'/dt' = V'^{-1}dV'/dt'$. The first term is for adiabatic cooling and the second term is for dilution. The particles confined into expanding volume are subject to adiabatic losses. To find the expressions for the loss rate one starts with the first law of thermodynamics

$$dU' = -PdV', \tag{A.2}$$

where for a mono-energetic population of particles the loss of internal energy is $U' = \frac{1}{\hat{\gamma}-1}n'k_BT'V'$ and $PV' = (\hat{\gamma}-1)U' = n'k_BT'V'$ is the pressure of the gas, k_B is the Boltzmann's constant, $\hat{\gamma}$ is the general adiabatic index where $\hat{\gamma} = 4/3$ is for a relativistic gas of particles/photons or $\hat{\gamma} = 5/3$ is for a non-relativistic gas of particles only, V' is the expanding volume, n' is the number density of particles and T' their temperature. Substituting and remembering that the average energy per particle is

$\frac{1}{\hat{\gamma}-1}k_B T'$

$$dU' = d(E'n'V') = -(\hat{\gamma}-1)n'E'dV'. \tag{A.3}$$

The total number of particle $N' = n'V'$, rewriting (A.3) and taking the rate:

$$\begin{aligned} \frac{dE'}{dt'} &= -\frac{(\hat{\gamma}-1)}{V'}E'\frac{dV'}{dt'}, \\ \frac{1}{E'}\frac{dE'}{dt'} &= \frac{d\ln E'}{dt'} = -(\hat{\gamma}-1)\frac{d\ln V'}{dt'}. \end{aligned} \tag{A.4}$$

To find the rate $d\ln V'/dt'$, first one can use the equation (6.7) to find dV'/dR,

$$\begin{aligned} \frac{dV'}{dR} &= \frac{3\pi R^2}{(3-k)\Gamma} - \frac{\pi R^3}{(3-k)\Gamma^2}\frac{d\Gamma}{dR} = \frac{3\pi R^2}{(3-k)\Gamma}\left(1 - \frac{1}{3}\frac{d\ln\Gamma}{d\ln R}\right), \\ \frac{dV'}{dR} &= \frac{3V'}{R}\left(1 - \frac{1}{3}\frac{d\ln\Gamma}{d\ln R}\right). \end{aligned} \tag{A.5}$$

Now one can compute,

$$\begin{aligned} \frac{dV'}{dt'} &= \frac{dV'}{dR}\frac{dR}{dt'} = \frac{dV'}{dR}\Gamma\beta c = \frac{3V'\Gamma\beta c}{R}\left(1 - \frac{1}{3}\frac{d\ln\Gamma}{d\ln R}\right), \\ \frac{1}{V'}\frac{dV'}{dt'} &= \frac{d\ln V'}{dt'} = \frac{3\Gamma\beta c}{R}\left(1 - \frac{1}{3}\frac{d\ln\Gamma}{d\ln R}\right), \end{aligned} \tag{A.6}$$

where $dR = \beta c d\hat{t} = \Gamma\beta c dt'$ and the adiabatic time scale is defined as $t'_{ad} = V'/(dV'/dt') = (d\ln V'/dt')^{-1}$. Substituting (A.6) in equation (A.4):

$$\frac{d\ln E'}{dt'} = -(\hat{\gamma}-1)\frac{3\Gamma\beta c}{R}\left(1 - \frac{1}{3}\frac{d\ln\Gamma}{d\ln R}\right). \tag{A.7}$$

With the last two expressions (i.e., equations (A.6) and (A.7)), one can find the form of the equation (A.1).

A.2 Compton scattering

For the Compton scattering density distribution rate, the treatment of Belmont (2009) is followed, where the Compton scattering cross section $d\sigma/dx$ (equations (27)-(39) of Belmont (2009)) is calculated exactly. Compton scattering is a collision process, so a treatment that describes a collision is followed (e.g., Belmont, 2009; Gill and Thompson, 2014)

$$\begin{aligned}\dot{N}'_{\pm,cs}(p) = &\int dp_0 N'_{\pm}(p_0) \int_{x_c(p_o)}^{\infty} dx_0 N'_{\gamma}(x_0) c \frac{d\sigma}{dp}(p_0, x_0 \rightarrow x(p)) \\ &- N'_{\pm}(p) \int_{x_c(p)}^{\infty} dx_0 N'_{\gamma}(x_0) c\sigma(p, x_0),\end{aligned} \tag{A.8}$$

$$\begin{aligned}\dot{N}'_{\gamma,cs}(x) = &\int dx_0 N'_{\gamma}(x_0) \int_{p_c(x_o)}^{\infty} dp_0 N'_{e}(p_0) c \frac{d\sigma}{dx}(p_0, x_0 \rightarrow x) \\ &- N'_{\gamma}(x) \int_{p_c(x)}^{\infty} dp_0 N'_{e}(p_0) c\sigma(p_0, x),\end{aligned} \tag{A.9}$$

where the term $x(p) = x_0 + \gamma_0(p_0) - \gamma(p)$ comes from energy conservation.

A.3 Pair production and annihilation

The processes of pair production and annihilation are collision processes. The equations to describe them are not limited by the grid resolution, these expressions are given by (e.g., Svensson, 1982; Böttcher and Schlickeiser, 1997; Gill and Thompson, 2014)

$$\dot{N}'_{\pm,pp}(p) = \int dx N'_{\gamma}(x) \int dx' N'_{\gamma}(x') R_{\gamma\gamma}(x, x' \rightarrow p), \tag{A.10}$$

$$\dot{N}'_{\pm,pa}(p) = - N'_{\pm}(p) \int dp' N'_{\pm}(p') R_{\pm}(p, p'), \tag{A.11}$$

$$\dot{N}'_{\gamma,pa}(x) = \int dp_+ N'_{+}(p_+) \int dp_- N'_{-}(p_-) R_{\pm}(p_+, p_- \rightarrow x), \tag{A.12}$$

$$\dot{N}'_{\gamma,pp}(x) = - N'_{\gamma}(x) \int dx' N_{\gamma}(x') R_{\gamma\gamma}(x, x'), \tag{A.13}$$

where

$$R_{\gamma\gamma}(x, x') = 2 \int dp R_{\gamma\gamma}(x, x' \to p), \tag{A.14}$$

$$R_{\pm}(p, p') = \frac{1}{2} \int dx R_{\pm}(p, p' \to x), \tag{A.15}$$

where $R_{\gamma\gamma}(x, x' \to p)$ is the rate of producing a lepton with momentum p upon the annihilation of two photons and, $R_{\pm}(p, p' \to x)$ is the rate of producing a photon with energy x when two photons annihilate each other.

A.4 Coulomb Scattering

The term $\dot{N}'_{\pm,\mathrm{coul}}$ in equation 6.1 is the density distribution rate. Analytic expressions describing the energy exchange and scattering of electrons undergoing Coulomb scattering are (Nayakshin and Melia, 1998; Vurm and Poutanen, 2009; Gill and Thompson, 2014):

$$A_{\pm,\mathrm{coul}}(p) = \int dp' N'_{\pm}(p') a_{\mathrm{coul}}(p, p'), \tag{A.16}$$

$$D_{\pm,\mathrm{coul}}(p) = \int dp' N'_{\pm}(p') d_{coul}(p, p'). \tag{A.17}$$

Bibliography

Abbott, B.P., Abbott, R., Abbott, T., Acernese, F., Ackley, K., Adams, C., Adams, T., Addesso, P., Adhikari, R., Adya, V., et al., 2017a. Gravitational waves and gamma-rays from a binary neutron star merger: Gw170817 and grb 170817a. The Astrophysical Journal Letters 848, L13.

Abbott, B.P., Abbott, R., Abbott, T., Acernese, F., Ackley, K., Adams, C., Adams, T., Addesso, P., Adhikari, R., Adya, V.B., et al., 2017b. Gw170817: observation of gravitational waves from a binary neutron star inspiral. Physical review letters 119, 161101.

Abdo, A., Ackermann, M., Ajello, M., Asano, K., Atwood, W.B., Axelsson, M., Baldini, L., Ballet, J., Barbiellini, G., Baring, M.G., et al., 2009. A limit on the variation of the speed of light arising from quantum gravity effects. Nature 462, 331–334.

Abramowitz, M., Stegun, I.A., 1964. Handbook of mathematical functions with formulas, graphs, and mathematical tables. volume 55. US Government printing office.

Acciari, V.A., Ansoldi, S., Antonelli, L.A., Engels, A.A., Baack, D., Babić, A., Banerjee, B., de Almeida, U.B., Barrio, J., González, J.B., et al., 2020. Teraelectronvolt emission from the \gamma-ray burst grb 190114c. arXiv preprint arXiv:2006.07249 .

Ackermann, M., Asano, K., Atwood, W., Axelsson, M., Baldini, L., Ballet, J., Barbiellini, G., Baring, M., Bastieri, D., Bechtol, K., et al., 2010. Fermi observations

of grb 090510: A short–hard gamma-ray burst with an additional, hard power-law component from 10 kev to gev energies. The Astrophysical Journal 716, 1178.

Ajello, M., Arimoto, M., Axelsson, M., Baldini, L., Barbiellini, G., Bastieri, D., Bellazzini, R., Bhat, P., Bissaldi, E., Blandford, R., et al., 2019. A decade of gamma-ray bursts observed by fermi-lat: the second grb catalog. The Astrophysical Journal 878, 52.

Andrade, U., Bengaly, C.A., Alcaniz, J.S., Capozziello, S., 2019. Revisiting the statistical isotropy of grb sky distribution. Monthly Notices of the Royal Astronomical Society 490, 4481–4488.

Arimoto, M., Asano, K., Ohno, M., Veres, P., Axelsson, M., Bissaldi, E., Tachibana, Y., Kawai, N., 2016. High-energy non-thermal and thermal emission from grb 141207a detected by fermi. The Astrophysical Journal 833, 139.

Asano, K., Mészáros, P., 2011. Spectral–temporal simulations of internal dissipation models of gamma-ray bursts. The Astrophysical Journal 739, 103.

Asano, K., Mészáros, P., 2012. Delayed onset of high-energy emissions in leptonic and hadronic models of gamma-ray bursts. The Astrophysical Journal 757, 115.

Asano, K., Murase, K., Toma, K., 2020. Probing particle acceleration through broadband early afterglow emission of magic gamma-ray burst grb 190114c. The Astrophysical Journal 905, 105.

Band, D., Matteson, J., Ford, L., Schaefer, B., Palmer, D., Teegarden, B., Cline, T., Briggs, M., Paciesas, W., Pendleton, G., et al., 1993. Batse observations of gamma-ray burst spectra. i-spectral diversity. The Astrophysical Journal 413, 281–292.

Barniol Duran, R., Bošnjak, Ž., Kumar, P., 2012. Inverse-compton cooling in klein–nishina regime and gamma-ray burst prompt spectrum. Monthly Notices of the Royal Astronomical Society 424, 3192–3200.

Belczynski, K., Perna, R., Bulik, T., Kalogera, V., Ivanova, N., Lamb, D.Q., 2006. A study of compact object mergers as short gamma-ray burst progenitors. The Astrophysical Journal 648, 1110.

Belmont, R., 2009. Numerical computation of isotropic compton scattering. Astronomy & Astrophysics 506, 589–599.

Beloborodov, A.M., 2000. On the efficiency of internal shocks in gamma-ray bursts. The Astrophysical Journal 539, L25–L28. URL: https://doi.org/10.1086%2F312830, doi:10.1086/312830.

Beloborodov, A.M., 2005. Afterglow emission from pair-loaded blast waves in gamma-ray bursts. The Astrophysical Journal 627, 346.

Beloborodov, A.M., Stern, B.E., Svensson, R., 2000. Power density spectra of gamma-ray bursts. The Astrophysical Journal 535, 158.

Benz, A.O., 2012. Plasma astrophysics: Kinetic processes in solar and stellar coronae. volume 184. Springer Science & Business Media.

Berger, E., Kulkarni, S., Frail, D., 2003. A standard kinetic energy reservoir in gamma-ray burst afterglows. The Astrophysical Journal 590, 379.

Beskin, G., Karpov, S., Bondar, S., Greco, G., Guarnieri, A., Bartolini, C., Piccioni, A., 2010. Fast optical variability of a naked-eye burst—manifestation of the periodic activity of an internal engine. The Astrophysical Journal Letters 719, L10.

Blandford, R.D., McKee, C.F., 1976. Fluid dynamics of relativistic blast waves. The Physics of Fluids 19, 1130–1138. URL: https://aip.scitation.org/doi/abs/10.1063/1.861619, doi:10.1063/1.861619, arXiv:https://aip.scitation.org/doi/pdf/10.1063/1.861619.

Blumenthal, G.R., Gould, R.J., 1970. Bremsstrahlung, synchrotron radiation, and compton scattering of high-energy electrons traversing dilute gases. Reviews of modern Physics 42, 237.

Böttcher, M., Dermer, C.D., 1998. High-energy gamma rays from ultra-high-energy cosmic-ray protons in gamma-ray bursts. The Astrophysical Journal 499, L131.

Böttcher, M., Schlickeiser, R., 1997. The pair production spectrum from photon-photon annihilation. arXiv preprint astro-ph/9703069 .

Briggs, M., Band, D., Kippen, R., Preece, R., Kouveliotou, C., Van Paradijs, J., Share, G., Murphy, R., Matz, S., Connors, A., et al., 1999. Observations of grb 990123 by the compton gamma ray observatory. The Astrophysical Journal 524, 82.

Burlon, D., Ghirlanda, G., Ghisellini, G., Greiner, J., Celotti, A., 2009. Time resolved spectral behavior of bright batse precursors. Astronomy & Astrophysics 505, 569–575.

Burrows, D.N., Romano, P., Falcone, A., Kobayashi, S., Zhang, B., Moretti, A., O'Brien, P.T., Goad, M.R., Campana, S., Page, K.L., et al., 2005. Bright x-ray flares in gamma-ray burst afterglows. Science 309, 1833–1835.

Cardone, V.F., Dainotti, M.G., Capozziello, S., Willingale, R., 2010. Constraining cosmological parameters by gamma-ray burst x-ray afterglow light curves. Monthly Notices of the Royal Astronomical Society 408, 1181–1186.

Chandrasekhar, S., 1943. Stochastic problems in physics and astronomy. Reviews of modern physics 15, 1.

Chang, J., Cooper, G., 1970. A practical difference scheme for fokker-planck equations. Journal of Computational Physics 6, 1–16.

Chiang, J., Dermer, C.D., 1999. Synchrotron and synchrotron self-compton emission and the blast-wave model of gamma-ray bursts. The Astrophysical Journal 512, 699.

Chincarini, G., Moretti, A., Romano, P., Falcone, A., Morris, D., Racusin, J., Campana, S., Covino, S., Guidorzi, C., Tagliaferri, G., et al., 2007. The first survey

of x-ray flares from gamma-ray bursts observed by swift: temporal properties and morphology. The Astrophysical Journal 671, 1903.

Crumley, P., Kumar, P., 2012. Hadronic models for lat prompt emission observed in fermi gamma-ray bursts. arXiv preprint arXiv:1210.7802 .

Dai, Z., Wu, X., 2003. Grb 030226 in a density-jump medium. The Astrophysical Journal 591, L21.

Derishev, E., Piran, T., 2019. The physical conditions of the afterglow implied by magic's sub-tev observations of grb 190114c. The Astrophysical Journal Letters 880, L27.

Derishev, E., Piran, T., 2021. Grb afterglow parameters in the era of tev observations: The case of grb 190114c. The Astrophysical Journal 923, 135.

Dermer, C.D., Menon, G., 2009. High energy radiation from black holes: gamma rays, cosmic rays, and neutrinos. volume 17. Princeton University Press.

Dichiara, S., Troja, E., Lipunov, V., Ricci, R., Oates, S., Butler, N., Liuzzo, E., Ryan, G., O'Connor, B., Cenko, S., et al., 2022. The early afterglow of grb 190829a. Monthly Notices of the Royal Astronomical Society 512, 2337–2349.

Drury, L.O., 1983. An introduction to the theory of diffusive shock acceleration of energetic particles in tenuous plasmas. Reports on Progress in Physics 46, 973.

Duran, R.B., Kumar, P., 2009. Adiabatic expansion, early x-ray data and the central engine in grbs. Monthly Notices of the Royal Astronomical Society 395, 955–961.

van Eerten, H., 2014. Self-similar relativistic blast waves with energy injection. Monthly Notices of the Royal Astronomical Society 442, 3495–3510.

Eichler, D., Livio, M., Piran, T., Schramm, D.N., 1989. Nucleosynthesis, neutrino bursts and γ-rays from coalescing neutron stars. Nature 340, 126–128.

Eichler, D., Waxman, E., 2005. The efficiency of electron acceleration in collisionless shocks and gamma-ray burst energetics. The Astrophysical Journal 627, 861.

Fan, Y., Wei, D., 2005. Late internal-shock model for bright x-ray flares in gamma-ray burst afterglows and grb 011121. Monthly Notices of the Royal Astronomical Society: Letters 364, L42–L46.

Ferenc, D., collaboration, M., et al., 2005. The magic gamma-ray observatory. Nuclear Instruments and Methods in Physics Research Section A: Accelerators, Spectrometers, Detectors and Associated Equipment 553, 274–281.

Fishman, G.J., Meegan, C.A., 1995. Gamma-ray bursts. Annual Review of Astronomy and Astrophysics 33, 415–458. URL: https://doi.org/10.1146/annurev.aa.33.090195.002215, doi:10.1146/annurev.aa.33.090195.002215, arXiv:https://doi.org/10.1146/annurev.aa.33.090195.002215.

Fishman, G.J., Meegan, C.A., Wilson, R.B., Brock, M.N., Horack, J.M., Kouveliotou, C., Howard, S., Paciesas, W.S., Briggs, M.S., Pendleton, G.N., et al., 1994. The first batse gamma-ray burst catalog. The Astrophysical Journal Supplement Series 92, 229–283.

Fraija, N., 2014. Gev–pev neutrino production and oscillation in hidden jets from gamma-ray bursts. Monthly Notices of the Royal Astronomical Society 437, 2187–2200.

Fraija, N., Dichiara, S., do ES Pedreira, A.C., Galvan-Gamez, A., Becerra, R., Duran, R.B., Zhang, B., 2019a. Analysis and modeling of the multi-wavelength observations of the luminous grb 190114c. The Astrophysical Journal Letters 879, L26.

Fraija, N., Dichiara, S., do ES Pedreira, A.C., Galvan-Gamez, A., Becerra, R., Montalvo, A., Montero, J., Kamenetskaia, B.B., Zhang, B., 2019b. Modeling the observations of grb 180720b: From radio to sub-tev gamma-rays. The Astrophysical Journal 885, 29.

Fraija, N., Duran, R.B., Dichiara, S., Beniamini, P., 2019c. Synchrotron self-compton as a likely mechanism of photons beyond the synchrotron limit in grb 190114c. The Astrophysical Journal 883, 162.

Fraija, N., Veres, P., Beniamini, P., Galvan-Gamez, A., Metzger, B., Duran, R.B., Becerra, R., 2021. On the origin of the multi-gev photons from the closest burst with intermediate luminosity: Grb 190829a. The Astrophysical Journal 918, 12.

Frail, D., Waxman, E., Kulkarni, S., 2000. A 450 day light curve of the radio afterglow of grb 970508: fireball calorimetry. The Astrophysical Journal 537, 191.

Fukushima, T., To, S., Asano, K., Fujita, Y., 2017. Temporal evolution of the gamma-ray burst afterglow spectrum for an observer: Gev–tev synchrotron self-compton light curve. The Astrophysical Journal 844, 92.

Ghisellini, G., Celotti, A., Fossati, G., Maraschi, L., Comastri, A., 1998. A theoretical unifying scheme for gamma-ray bright blazars. Monthly Notices of the Royal Astronomical Society 301, 451–468.

Gill, R., Granot, J., 2018a. Afterglow imaging and polarization of misaligned structured grb jets and cocoons: breaking the degeneracy in grb 170817a. Monthly Notices of the Royal Astronomical Society 478, 4128–4141.

Gill, R., Granot, J., 2018b. The effect of pair cascades on the high-energy spectral cut-off in gamma-ray bursts. Monthly Notices of the Royal Astronomical Society: Letters 475, L1–L5.

Gill, R., Granot, J., 2022. Gamma-ray bursts at tev energies: Theoretical considerations. Galaxies 10, 74.

Gill, R., Granot, J., Beniamini, P., 2020. Grb spectrum from gradual dissipation in a magnetized outflow. Monthly Notices of the Royal Astronomical Society 499, 1356–1372.

Gill, R., Thompson, C., 2014. Non-thermal gamma-ray emission from delayed pair breakdown in a magnetized and photon-rich outflow. The Astrophysical Journal 796, 81.

Goldstein, A., Burgess, J.M., Preece, R.D., Briggs, M.S., Guiriec, S., van der Horst, A.J., Connaughton, V., Wilson-Hodge, C.A., Paciesas, W.S., Meegan, C.A., et al., 2012. The fermi gbm gamma-ray burst spectral catalog: the first two years. The Astrophysical Journal Supplement Series 199, 19.

González, M., Dingus, B., Kaneko, Y., Preece, R.D., Dermer, C.D., Briggs, M., 2003. A γ-ray burst with a high-energy spectral component inconsistent with the synchrotron shock model. Nature 424, 749–751.

Granot, J., Sari, R., 2002. The shape of spectral breaks in gamma-ray burst afterglows. The Astrophysical Journal 568, 820.

Gruber, D., Goldstein, A., von Ahlefeld, V.W., Bhat, P.N., Bissaldi, E., Briggs, M.S., Byrne, D., Cleveland, W.H., Connaughton, V., Diehl, R., et al., 2014. The fermi gbm gamma-ray burst spectral catalog: four years of data. The Astrophysical Journal Supplement Series 211, 12.

Guiriec, S., Kouveliotou, C., Daigne, F., Zhang, B., Hascoët, R., Nemmen, R., Thompson, D., Bhat, P., Gehrels, N., Gonzalez, M., et al., 2015. Toward a better understanding of the grb phenomenon: a new model for grb prompt emission and its effects on the new lint–epeak, irest, nt relation. The Astrophysical Journal 807, 148.

Hajela, A., Margutti, R., Alexander, K., Kathirgamaraju, A., Baldeschi, A., Guidorzi, C., Giannios, D., Fong, W., Wu, Y., MacFadyen, A., et al., 2019. Two years of nonthermal emission from the binary neutron star merger gw170817: rapid fading of the jet afterglow and first constraints on the kilonova fastest ejecta. The Astrophysical Journal Letters 886, L17.

Harrison, F., Bloom, J., Frail, D.A., Sari, R., Kulkarni, S.R., Djorgovski, S., Axelrod, T., Mould, J., Schmidt, B.P., Wieringa, M.H., et al., 1999. Optical and radio observations of the afterglow from grb 990510: Evidence for a jet. The Astrophysical Journal 523, L121.

Horváth, I., Hakkila, J., Bagoly, Z., 2014. Possible structure in the grb sky distribution at redshift two. Astronomy & Astrophysics 561, L12.

Ioka, K., Kobayashi, S., Zhang, B., 2005. Variabilities of gamma-ray burst afterglows: long-acting engine, anisotropic jet, or many fluctuating regions? The Astrophysical Journal 631, 429.

Joshi, J.C., Chand, V., Razzaque, S., 2023. Synchrotron and synchrotron self-compton emission components in grbs detected at very high energies, in: The Sixteenth Marcel Grossmann Meeting on Recent Developments in Theoretical and Experimental General Relativity, Astrophysics and Relativistic Field Theories: Proceedings of the MG16 Meeting on General Relativity Online; 5–10 July 2021, World Scientific. pp. 3009–3016.

Joshi, J.C., Razzaque, S., 2021. Modelling synchrotron and synchrotron self-compton emission of gamma-ray burst afterglows from radio to very-high energies. Monthly Notices of the Royal Astronomical Society 505, 1718–1729.

Katz, J., 1992. Two populations and models of gamma ray bursts. arXiv preprint astro-ph/9212006 .

Konopelko, A., Plyasheshnikov, A., 2000. Altai: computational code for the simulations of tev air showers as observed with the ground-based imaging atmospheric cherenkov telescopes. Nuclear Instruments and Methods in Physics Research Section A: Accelerators, Spectrometers, Detectors and Associated Equipment 450, 419–429.

Kouveliotou, C., Meegan, C.A., Fishman, G.J., Bhat, N.P., Briggs, M.S., Koshut, T.M., Paciesas, W.S., Pendleton, G.N., 1993. Identification of two classes of gamma-ray bursts. The Astrophysical Journal 413, L101–L104.

Kumar, P., Granot, J., 2003. The evolution of a structured relativistic jet and gamma-ray burst afterglow light curves. The Astrophysical Journal 591, 1075. URL: https://dx.doi.org/10.1086/375186, doi:10.1086/375186.

Kumar, P., Panaitescu, A., 2000. Afterglow emission from naked gamma-ray bursts. The Astrophysical Journal 541, L51.

Kumar, P., Piran, T., 2000. Some observational consequences of gamma-ray burst shock models. The Astrophysical Journal 532, 286.

Kumar, P., Zhang, B., 2015. The physics of gamma-ray bursts & relativistic jets. Physics Reports 561, 1–109. URL: https://www.sciencedirect.com/science/article/pii/S0370157314003846, doi:https://doi.org/10.1016/j.physrep.2014.09.008. the physics of gamma-ray bursts & relativistic jets.

Lamb, D.Q., Reichart, D.E., 2000. Gamma-ray bursts as a probe of the very high redshift universe. The Astrophysical Journal 536, 1.

Lazzati, D., 2005. Precursor activity in bright, long batse gamma-ray bursts. Monthly Notices of the Royal Astronomical Society 357, 722–731.

Lazzati, D., Begelman, M.C., 2010. Non-thermal emission from the photospheres of gamma-ray burst outflows. i. high-frequency tails. The Astrophysical Journal 725, 1137.

Lazzati, D., Perna, R., 2007. X-ray flares and the duration of engine activity in gamma-ray bursts. Monthly Notices of the Royal Astronomical Society: Letters 375, L46–L50.

Lazzati, D., Rossi, E., Covino, S., Ghisellini, G., Malesani, D., 2002. The afterglow of grb 021004: surfing on density waves. Astronomy & Astrophysics 396, L5–L9.

Li, L., Wang, X.G., Zheng, W., Pozanenko, A.S., Filippenko, A.V., Qin, S., Wang, S.Q., Jiang, L.Y., Li, J., Lin, D.B., et al., 2020. Grb 140423a: A case of stellar wind to interstellar medium transition in the afterglow. The Astrophysical Journal 900, 176.

Liang, E., Zhang, B., O'Brien, P., Willingale, R., Angelini, L., Burrows, D., Campana, S., Chincarini, G., Falcone, A., Gehrels, N., et al., 2006. Testing the curvature effect

and internal origin of gamma-ray burst prompt emissions and x-ray flares with swift data. The Astrophysical Journal 646, 351.

Liddle, A.R., 1998. An introduction to cosmological inflation. High energy physics and cosmology , 260.

Lipkin, Y.M., Ofek, E.O., Gal-Yam, A., Leibowitz, E., Poznanski, D., Kaspi, S., Polishook, D., Kulkarni, S.R., Fox, D., Berger, E., et al., 2004. The detailed optical light curve of grb 030329. The Astrophysical Journal 606, 381.

Longair, M.S., 2010. High energy astrophysics. Cambridge university press.

Lü, H.J., Zhang, B., Lei, W.H., Li, Y., Lasky, P.D., 2015. The millisecond magnetar central engine in short grbs. The Astrophysical Journal 805, 89.

Maral, G., 2004. VSAT Networks. Wiley series in communication and distributed systems, Wiley. URL: https://books.google.com.mx/books?id=CMx5HQ1Mr_UC.

Medvedev, M.V., 2000. Theory of "jitter" radiation from small-scale random magnetic fields and prompt emission from gamma-ray burst shocks. The Astrophysical Journal 540, 704.

Medvedev, M.V., Loeb, A., 1999. Generation of Magnetic Fields in the Relativistic Shock of Gamma-Ray Burst Sources. apj 526, 697–706. doi:10.1086/308038, arXiv:astro-ph/9904363.

Medvedev, M.V., Loeb, A., 1999. Generation of magnetic fields in the relativistic shock of gamma-ray burst sources. The Astrophysical Journal 526, 697.

Mészáros, P., 2001. Gamma-ray bursts: accumulating afterglow implications, progenitor clues, and prospects. Science 291, 79–84.

Mészáros, P., Kobayashi, S., Razzaque, S., Zhang, B., 2003. High energy photons, neutrinos and gravitational waves from gamma-ray bursts. arXiv preprint astro-ph/0305066 .

Meszaros, P., Rees, M., 1993. Relativistic fireballs and their impact on external matter-models for cosmological gamma-ray bursts. The Astrophysical Journal 405, 278–284.

Mészáros, P., Rees, M.J., 1994. Delayed gev emission from cosmological gamma-ray bursts: Impact of a relativistic wind on external matter. Monthly Notices of the Royal Astronomical Society 269, L41–L43.

Moiseev, S., Sagdeev, R., 1963. Collisionless shock waves in a plasma in a weak magnetic field. Journal of Nuclear Energy. Part C, Plasma Physics, Accelerators, Thermonuclear Research 5, 43.

Murase, K., Asano, K., Terasawa, T., Meszaros, P., 2012. The role of stochastic acceleration in the prompt emission of gamma-ray bursts: application to hadronic injection. The Astrophysical Journal 746, 164.

Mészáros, P., Rees, M.J., 1997. Optical and long-wavelength afterglow from gamma-ray bursts. The Astrophysical Journal 476, 232.

Nakar, E., 2007. Short-hard gamma-ray bursts. Physics Reports 442, 166–236.

Nakar, E., 2015. A unified picture for low-luminosity and long gamma-ray bursts based on the extended progenitor of llgrb 060218/sn 2006aj. The Astrophysical Journal 807, 172.

Nakar, E., Ando, S., et al., 2009. Klein–nishina effects on optically thin synchrotron and synchrotron self-compton spectrum. The Astrophysical Journal 703, 675.

Nakar, E., Granot, J., 2007. Smooth light curves from a bumpy ride: relativistic blast wave encounters a density jump. Monthly Notices of the Royal Astronomical Society 380, 1744–1760. URL: https://doi.org/10.1111/j.1365-2966.2007.12245.x, doi:10.1111/j.1365-2966.2007.12245.x.

Narayan, R., Paczyński, B., Piran, T., 1992. Gamma-ray bursts as the death throes of massive binary stars. arXiv preprint astro-ph/9204001 .

NASA's Goddard Space Flight Center, 2023. Nasa's goddard space flight center. URL: `https://www.nasa.gov/goddard`.

Nava, L., Sironi, L., Ghisellini, G., Celotti, A., Ghirlanda, G., 2013. Afterglow emission in gamma-ray bursts–i. pair-enriched ambient medium and radiative blast waves. Monthly Notices of the Royal Astronomical Society 433, 2107–2121.

Nayakshin, S., Melia, F., 1998. Self-consistent fokker-planck treatment of particle distributions in astrophysical plasmas. The Astrophysical Journal Supplement Series 114, 269.

Nousek, J., Kouveliotou, C., Grupe, D., Page, K., Granot, J., Ramirez-Ruiz, E., Patel, S., Burrows, D., Mangano, V., Barthelmy, S., et al., 2006. Evidence for a canonical gamma-ray burst afterglow light curve in the swift xrt data. The Astrophysical Journal 642, 389.

Paczyński, B., 1998. Gamma-ray bursts as hypernovae, in: AIP Conference Proceedings, American Institute of Physics. pp. 783–787.

Paczynski, B., Rhoads, J.E., 1993. Radio transients from gamma-ray bursters. arXiv preprint astro-ph/9307024 .

Panaitescu, A., 2007. Swift gamma-ray burst afterglows and the forward-shock model. Monthly Notices of the Royal Astronomical Society 379, 331–342.

Panaitescu, A., Kumar, P., 2000. Analytic light curves of gamma-ray burst afterglows: homogeneous versus wind external media. The Astrophysical Journal 543, 66.

Pennanen, T., Vurm, I., Poutanen, J., 2014. Simulations of gamma-ray burst afterglows with a relativistic kinetic code. Astronomy & Astrophysics 564, A77.

Petropoulou, M., Mastichiadis, A., 2009. On the multiwavelength emission from gamma ray burst afterglows. Astronomy & Astrophysics 507, 599–610.

Pe'er, A., Mészáros, P., Rees, M.J., 2006. The observable effects of a photospheric component on grb and xrf prompt emission spectrum. The Astrophysical Journal 642, 995.

Piran, T., 2005. The physics of gamma-ray bursts. Reviews of Modern Physics 76, 1143.

Piran, T., Halpern, J., et al., 1999. Jets in gamma-ray bursts. The Astrophysical Journal 519, L17.

Racusin, J.L., Karpov, S., Sokolowski, M., Granot, J., Wu, X.F., Pal'Shin, V., Covino, S., Van Der Horst, A.J., Oates, S., Schady, P., et al., 2008. Broadband observations of the naked-eye gamma-ray burst grb 080319b. Nature 455, 183–188.

Ravasio, M., Oganesyan, G., Salafia, O.S., Ghirlanda, G., Ghisellini, G., Branchesi, M., Campana, S., Covino, S., Salvaterra, R., 2019. Grb 190114c: from prompt to afterglow? Astronomy & Astrophysics 626, A12.

Razzaque, S., 2010. A leptonic–hadronic model for the afterglow of gamma-ray burst 090510. The Astrophysical Journal Letters 724, L109.

Resmi, L., Zhang, B., 2012. Gamma-ray burst prompt emission variability in synchrotron and synchrotron self-compton light curves. Monthly Notices of the Royal Astronomical Society 426, 1385–1395.

Rhoads, J.E., 1999. The dynamics and light curves of beamed gamma-ray burst afterglows. The Astrophysical Journal 525, 737.

Rybicki, G.B., Lightman, A.P., 1991. Radiative processes in astrophysics. John Wiley & Sons.

Sahu, S., Fortín, C.E.L., 2020. Origin of sub-tev afterglow emission from gamma-ray bursts grb 190114c and grb 180720b. The Astrophysical Journal Letters 895, L41.

Sahu, S., Polanco, I.A.V., Rajpoot, S., 2022. Very high-energy afterglow emission of grb 190829a: Evidence for its hadronic origin? The Astrophysical Journal 929, 70.

Sakamoto, T., Hullinger, D., Sato, G., Yamazaki, R., Barbier, L., Barthelmy, S.D., Cummings, J.R., Fenimore, E.E., Gehrels, N., Krimm, H.A., Lamb, D.Q., Markwardt, C.B., Osborne, J.P., Palmer, D.M., Parsons, A.M., Stamatikos, M., Tueller, J., 2008. Global properties of x-ray flashes and x-ray-rich gamma-ray bursts observed by swift. The Astrophysical Journal 679, 570. URL: https://dx.doi.org/10.1086/586884, doi:10.1086/586884.

Salafia, O.S., Ravasio, M.E., Yang, J., An, T., Orienti, M., Ghirlanda, G., Nava, L., Giroletti, M., Mohan, P., Spinelli, R., et al., 2022. Multiwavelength view of the close-by grb 190829a sheds light on gamma-ray burst physics. The Astrophysical Journal Letters 931, L19.

Santana, R., Duran, R.B., Kumar, P., 2014. Magnetic fields in relativistic collisionless shocks. The Astrophysical Journal 785, 29.

Sari, R., Esin, A.A., 2001. On the synchrotron self-compton emission from relativistic shocks and its implications for gamma-ray burst afterglows. The Astrophysical Journal 548, 787.

Sari, R., Piran, T., 1997. Cosmological gamma-ray bursts: internal versus external shocks. Monthly Notices of the Royal Astronomical Society 287, 110–116.

Sari, R., Piran, T., Narayan, R., 1998. Spectra and light curves of gamma-ray burst afterglows,. ApJ 497.

Sironi, L., Goodman, J., 2007. Production of magnetic energy by macroscopic turbulence in grb afterglows. The Astrophysical Journal 671, 1858. URL: https://dx.doi.org/10.1086/523636, doi:10.1086/523636.

Sironi, L., Spitkovsky, A., 2009. Particle acceleration in relativistic magnetized collisionless pair shocks: dependence of shock acceleration on magnetic obliquity. The Astrophysical Journal 698, 1523.

Sironi, L., Spitkovsky, A., 2010. Particle acceleration in relativistic magnetized collisionless electron–ion shocks. The Astrophysical Journal 726, 75.

Stanek, K.Z., Matheson, T., Garnavich, P., Martini, P., Berlind, P., Caldwell, N., Challis, P., Brown, W., Schild, R., Krisciunas, K., et al., 2003. Spectroscopic discovery of the supernova 2003dh associated with grb 030329. The Astrophysical Journal 591, L17.

Svensson, R., 1982. The pair annihilation process in relativistic plasmas. The Astrophysical Journal 258, 321–334.

Thompson, C., Duncan, R.C., 1993. Neutron star dynamos and the origins of pulsar magnetism. The Astrophysical Journal 408, 194–217.

Thompson, C., Madau, P., 2000. Relativistic winds from compact gamma-ray sources. ii. pair loading and radiative acceleration in gamma-ray bursts. The Astrophysical Journal 538, 105.

Uhm, Z.L., 2011. A semi-analytic formulation for relativistic blast waves with a long-lived reverse shock. The Astrophysical Journal 733, 86. URL: https://dx.doi.org/10.1088/0004-637X/733/2/86, doi:10.1088/0004-637X/733/2/86.

Vedrenne, G., Atteia, J.L., 2009. Gamma-ray bursts: The brightest explosions in the universe. Springer Science & Business Media.

Veres, P., Bhat, P., Briggs, M., Cleveland, W., Hamburg, R., Hui, C., Mailyan, B., Preece, R., Roberts, O., von Kienlin, A., et al., 2019. Observation of inverse compton emission from a long γ-ray burst. Nature 575, 459–463.

Vianello, G., Gill, R., Granot, J., Omodei, N., Cohen-Tanugi, J., Longo, F., 2018. The bright and the slow—grbs 100724b and 160509a with high-energy cutoffs at 100 mev. The Astrophysical Journal 864, 163.

Vurm, I., Beloborodov, A.M., Poutanen, J., 2011. Gamma-ray bursts from magnetized collisionally heated jets. The Astrophysical Journal 738, 77.

Vurm, I., Poutanen, J., 2009. Time-dependent modeling of radiative processes in hot magnetized plasmas. The Astrophysical Journal 698, 293.

Wang, X.G., Zhang, B., Liang, E.W., Gao, H., Li, L., Deng, C.M., Qin, S.M., Tang, Q.W., Kann, D.A., Ryde, F., et al., 2015. How bad or good are the external forward shock afterglow models of gamma-ray bursts? The Astrophysical Journal Supplement Series 219, 9.

Wang, X.Y., Dai, Z., Lu, T., 2001. The inverse compton emission spectra in the very early afterglows of gamma-ray bursts. The Astrophysical Journal 556, 1010.

Wang, X.Y., Liu, R.Y., Zhang, H.M., Xi, S.Q., Zhang, B., 2019. Synchrotron self-compton emission from external shocks as the origin of the sub-tev emission in grb 180720b and grb 190114c. The Astrophysical Journal 884, 117.

Waxman, E., 2006. Gamma-ray bursts and collisionless shocks. Plasma Physics and Controlled Fusion 48, B137.

Weaver, R., McCray, R., Castor, J., Shapiro, P., Moore, R., 1977. Interstellar bubbles. ii-structure and evolution. The Astrophysical Journal 218, 377–395.

Weisstein, Eric W., 2023. "relative error". URL: `https://mathworld.wolfram.com/RelativeError.html`.

Wijers, R., Galama, T., 1999. Physical parameters of grb 970508 and grb 971214 from their afterglow synchrotron emission. The Astrophysical Journal 523, 177.

Wijers, R.A.M.J., Rees, M.J., Mészáros, P., 1997. Shocked by GRB 970228: the afterglow of a cosmological fireball. Monthly Notices of the Royal Astronomical Society 288, L51–L56. URL: `https://doi.org/10.1093/mnras/288.4.L51`, doi:`10.1093/mnras/288.4.L51`.

Woosley, S.E., 1993. Gamma-ray bursts from stellar mass accretion disks around black holes. Astrophysical Journal, Part 1 (ISSN 0004-637X), vol. 405, no. 1, p. 273-277. 405, 273–277.

Yamasaki, S., Piran, T., 2022. Analytic modelling of synchrotron self-compton spectra: Application to grb 190114c. Monthly Notices of the Royal Astronomical Society 512, 2142–2153.

Yamazaki, R., Ioka, K., Nakamura, T., 2004. A unified model of short and long gamma-ray bursts, x-ray-rich gamma-ray bursts, and x-ray flashes. The Astrophysical Journal 607, L103.

Zafar, T., 2011. Spectroscopy of high redshift sightlines. Ph. D. Thesis .

Zhang, B., 2018. The Physics of Gamma-Ray Bursts. Cambridge University Press. URL: https://books.google.com.mx/books?id=isd6DwAAQBAJ.

Zhang, B., Fan, Y.Z., Dyks, J., Kobayashi, S., Mészáros, P., Burrows, D.N., Nousek, J.A., Gehrels, N., 2006. Physical processes shaping gamma-ray burst x-ray afterglow light curves: theoretical implications from the swift x-ray telescope observations. The Astrophysical Journal 642, 354.

Zhang, B., Kobayashi, S., 2005. Gamma-ray burst early afterglows: reverse shock emission from an arbitrarily magnetized ejecta. The Astrophysical Journal 628, 315.

Zhang, B., Lu, R.J., Liang, E.W., Wu, X.F., 2012. Grb 110721a: Photosphere "death line" and the physical origin of the grb band function. The Astrophysical Journal Letters 758, L34.

Zhang, B., Mészáros, P., 2001. High-energy spectral components in gamma-ray burst afterglows. The Astrophysical Journal 559, 110.

Zhang, B., Meszaros, P., 2004. Gamma-ray bursts: progress, problems & prospects. International Journal of Modern Physics A 19, 2385–2472.

Zhang, B., Mészáros, P., 2002. Gamma-ray bursts with continuous energy injection and their afterglow signature. The Astrophysical Journal 566, 712.

Zhang, B.B., Zhang, B., Castro-Tirado, A.J., 2016. Central engine memory of gamma-ray bursts and soft gamma-ray repeaters. The Astrophysical Journal Letters 820, L32.

Zhang, B.B., Zhang, B., Liang, E.W., Fan, Y.Z., Wu, X.F., Pe'er, A., Maxham, A., Gao, H., Dong, Y.M., 2011. A comprehensive analysis of fermi gamma-ray burst data. i. spectral components and the possible physical origins of lat/gbm grbs. The Astrophysical Journal 730, 141.

Zhang, B.T., Murase, K., Veres, P., Mészáros, P., 2021. External inverse-compton emission from low-luminosity gamma-ray bursts: Application to grb 190829a. The Astrophysical Journal 920, 55.

Zhang, H., Christie, I., Petropoulou, M., Rueda-Becerril, J.M., Giannios, D., 2020. Inverse compton signatures of gamma-ray burst afterglows. Monthly Notices of the Royal Astronomical Society 496, 974–986.

Zhang, Z.B., Choi, C.S., 2008. An analysis of the durations of swift gamma-ray bursts. Astronomy & Astrophysics 484, 293–297.